Journal of Computational and Applied Mathematics 378 (2020) 112905

Contents lists available at ScienceDirect

Journal of Computational and Applied Mathematics

journal homepage: www.elsevier.com/locate/cam

Efficient numerical scheme for a penalized Allen–Cahn type Ohta–Kawasaki phase-field model for diblock copolymers

Jun Zhang [a], Chuanjun Chen [b,*], Xiaofeng Yang [c], Kejia Pan [d]

[a] Computational Mathematics Research Center, Guizhou University of Finance and Economics, Guiyang 550025, China
[b] School of Mathematics and Information Sciences, Yantai University, Yantai 264005, China
[c] Department of Mathematics, University of South Carolina, Columbia, SC 29208, USA
[d] School of Mathematics and Statistics, Central South University, Changsha, 410083, China

ARTICLE INFO

Article history:
Received 11 September 2019
Received in revised form 24 March 2020

Keywords:
Phase-field
S-SAV
Diblock copolymer
Allen–Cahn
Second-order
Unconditional energy stability

ABSTRACT

In this paper, we develop an unconditionally energy stable, second-order accurate time marching scheme for solving a penalized Allen–Cahn type Ohta–Kawasaki phase-field model for diblock copolymers, where the total free energy of the system consists of the double-well potential, the nonlocal Ohta–Kawasaki free energy functional, and a penalization potential to enforce the conservation of the modified volume approximately. The developed scheme combines the SAV (scalar auxiliary variable) approach with the stabilization technique, where a crucial linear stabilization term is added to enhance the stability while using the large time steps. The scheme is very easy-to-implement and one only needs to solve two decoupled elliptic equations with constant coefficients at each time step. We further prove the unconditional energy stability of the scheme rigorously and demonstrate the stability and the accuracy of the developed scheme numerically through simulating numerous numerical examples in 2D and 3D.

1. Introduction

In this paper, we consider numerical approximations for solving a penalized Allen–Cahn type Ohta–Kawasaki phase-field model for diblock copolymers that was recently developed in [1]. A diblock copolymer is a polymer consisting of two types of monomers which are arranged such that there is a chain of each monomer, and those two chains are grafted together to form a single copolymer chain. The phase-field type model for diblock copolymers usually adopts a scalar phase field variable to denote the difference between the local volume fractions of two monomers, cf. [2–8]. By postulating total free energy that incorporates some specific potentials such as the well-known nonlocal Ohta–Kawasaki potential, the governing model is derived by using the variational approach in a certain metric to minimize it. The commonly-used phase-field model is derived by using the variational approach in H^{-1}-space (or called the Cahn–Hilliard dynamics). This is because the phase-field variable is interpreted as the local volume fraction of the two monomers in this particular surroundings and thus it is expected to be conserved with the time which can be easily fulfilled by using the H^{-1} gradient flow approach [2,9–13].

Remarkably, we recall that there is another well-known gradient flow approach in the phase-field modeling, the so-called Allen–Cahn dynamics (the variational approach in the L^2-space). The Allen–Cahn type model usually generates a PDE system which is second-order less than the Cahn–Hilliard type model, thus it is relatively easier to solve numerically.

* Corresponding author.
E-mail addresses: jzhang@mail.gufe.edu.cn (J. Zhang), cjchen@ytu.edu.cn (C. Chen), xfyang@math.sc.edu (X. Yang), kejiapan@csu.edu.cn (K. Pan).

https://doi.org/10.1016/j.cam.2020.112905
0377-0427/

However, the volume fraction in the Allen–Cahn model is not conserved with the time [14,15]. In [1], Xu and Zhao proposed an Allen–Cahn type phase-field model for diblock copolymers where the function in the nonlocal Ohta–Kawasaki potential is changed to a nonlinear fifth-order polynomial instead of the linear polynomial since a much better hyperbolic tangent profile can be generated and the interfacial structures can be described more accurately in turn. The model further adopts a strong nonlinear penalization potential to conserve the "modified" volume approximately. Hence, even though the order of the system is decreased from fourth-order (Cahn–Hilliard) to be second-order by using Allen–Cahn dynamics, this new model presents more numerical challenges on how to design proper temporal discretizations for numerous nonlinear and nonlocal terms to obtain stable and accurate schemes.

To develop efficient algorithms for solving this new Allen–Cahn diblock copolymer model, traditional temporal discretization approaches like simple implicit [15], explicit [14,16–19], convex splitting [20,21], or other various tricky Taylor expansions to discretize these terms [22–24], will produce either non-linear schemes which need some efficient iterative solvers or schemes which might fail to preserve energy stability [16,25]. In [1], the authors develop an energy stable scheme based on the linear stabilized explicit approach where all nonlinear terms are treated explicitly and two linear stabilizers are added for the stability reason. The scheme is very efficient, however, it is only first-order accurate in time. It is worth mentioning that the recently developed IEQ (Invariant Energy Quadratization) and SAV (Scalar Auxiliary Variable) methods (cf. [26–32]) can produce linear and provably unconditional energy stable schemes for gradient flow models. However, when the stiffness of the system is very high, the obtained linear/linearized system could be ill-conditioned thereby these methods lead to very costly iterations or cause the loss of accuracy, cf. the accuracy/stability tests shown in Figs. 4.2, 4.3 and 4.9.

The paper aims to develop a second-order accurate numerical scheme with more desired properties such as easy-to-implement and unconditionally energy stable. To this end, we combine the SAV approach [28,31,32] with the stabilization technique to arrive the stabilized-SAV approach, where an extra linear stabilization term is added to enhance the stability while using large time steps. Meanwhile, the implementation procedure for the developed scheme is very simple and one only needs to solve two decoupled, linear elliptic equations with constant coefficients at each time step. We present the rigorous proof of the unconditional energy stability and demonstrate the stability and accuracy numerically through the comparison with the non-stabilized SAV scheme, and the first-order stabilized explicit scheme in simulating numerous numerical examples in 2D and 3D.

The rest of the paper is organized as follows. In Section 2, we give a brief introduction of the governing PDE system for penalized Allen–Cahn phase-field diblock copolymer model. In Section 3, we develop the numerical scheme with second-order temporal accuracy to solve this model. Various 2D and 3D numerical experiments are given in Section 4 to show the accuracy and efficiency of the proposed numerical scheme. Finally, some concluding remarks are given in Section 5.

2. Model equations

We now give a brief introduction to the penalized Allen–Cahn diblock copolymer model proposed in [1]. We consider a system that consists of molecules of two monomers, where the state of the system is described by the local volume fraction of these two components, $\phi(\boldsymbol{x}, t)$ with $\boldsymbol{x} \in \Omega^d$, $d = 2, 3$ and time t. The total free energy $E(\phi)$ is postulated as

$$E(\phi) = \underbrace{\int_\Omega \left(\frac{\epsilon^2}{2}|\nabla\phi|^2 + F(\phi)\right) d\boldsymbol{x}}_{\text{I}} + \underbrace{\frac{\alpha\epsilon^2}{2}\int_\Omega \left|\nabla\left((-\Delta)^{-1}(g(\phi) - \bar{g}(\phi))\right)\right|^2 d\boldsymbol{x}}_{\text{II}} + \underbrace{\frac{\beta\epsilon^2}{2}\left(\int_\Omega g(\phi)d\boldsymbol{x} - \int_\Omega g(\phi_0)d\boldsymbol{x}\right)^2}_{\text{III}}, \tag{2.1}$$

where ϵ, α, β are all positive parameters. We give a brief introduction for the total free energy (2.1) as follows.

Part I is the well-known mixing energy potential for the phase-field model. The linear gradient part contributes to the hydrophilic type (tendency of mixing) of interactions and the double-well potential $F(\phi) = \frac{1}{4}\phi^2(\phi - 1)^2$ represents the hydrophobic type (tendency of separation) of interactions. The parameter ϵ is related to the width of the interface. As the consequence of the competition between the two types of interactions, the equilibrium configuration will include a diffusive interface.

Part II is the so-called nonlocal Ohta–Kawasaki potential, α is a positive parameter to characterize the nonlocal potential and the molecular chain length. The inverse Laplace operator $\psi = (-\Delta)^{-1}\phi$ is defined as

$$\begin{cases} -\Delta\psi = \phi, \\ \displaystyle\int_\Omega \psi d\boldsymbol{x} = 0, \end{cases} \tag{2.2}$$

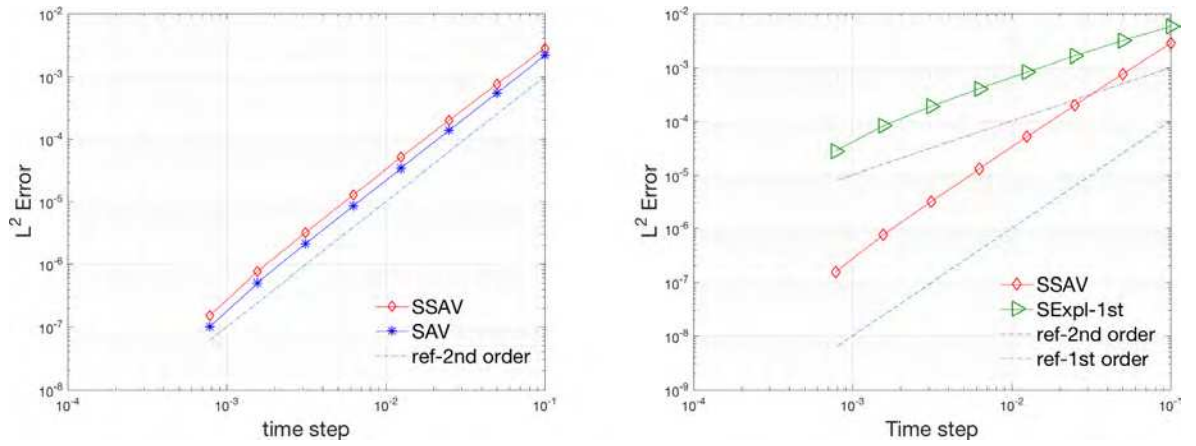

Fig. 4.1. The L^2 numerical errors for the phase field variable ϕ that are computed using the three schemes with various temporal resolutions where (a) SSAV and SAV, (b) SSAV and SExpl-1st. The order parameters are set as $(M, \alpha, \beta, \epsilon) = (6e{-}2, 1e{-}2, 1e{-}2, 6e{-}2)$ (low stiffness case). (Note: the two straight lines labeled as ref-2nd-order and ref-1st-order are the standard lines representing the second-order accuracy and first-order accuracy, respectively.).

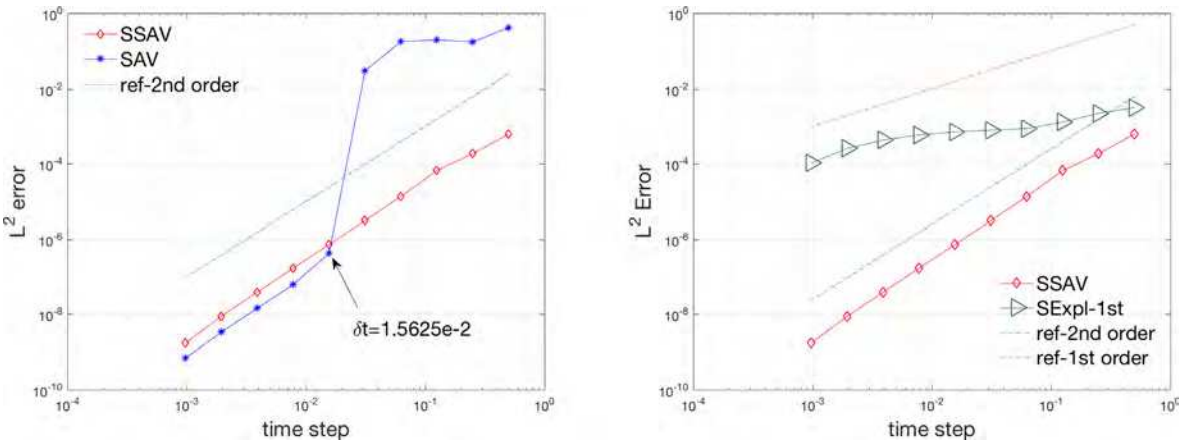

Fig. 4.2. The L^2 numerical errors for the phase field variable ϕ that are computed using the three schemes with various temporal resolutions where (a) SSAV and SAV, (b) SSAV and SExpl-1st. The order parameters are set as $(M, \alpha, \beta, \epsilon) = (1e1, 1e3, 1e5, 2e{-}2)$ (high stiffness case).

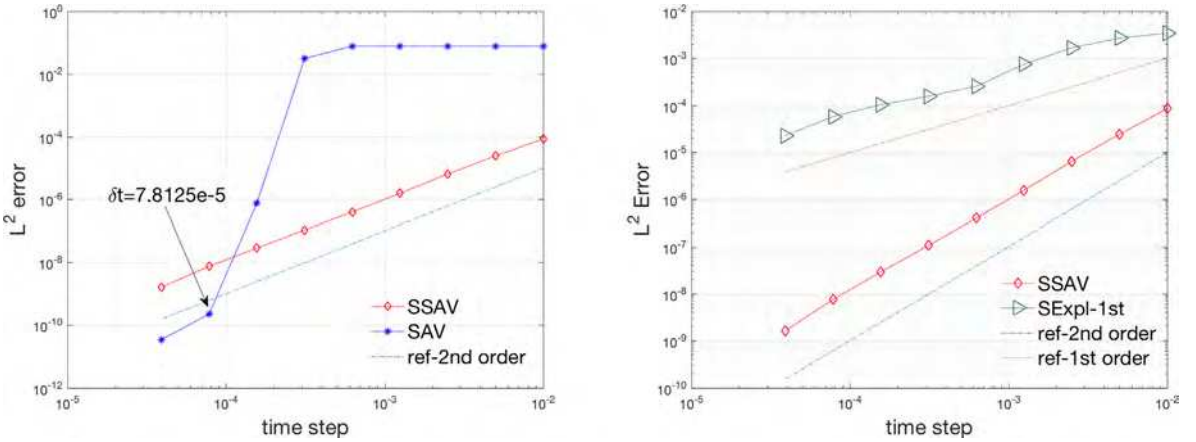

Fig. 4.3. The L^2 numerical errors for the phase field variable ϕ that are computed using the three schemes with various temporal resolutions where (a) SSAV and SAV, (b) SSAV and SExpl-1st. The order parameters are set as $(M, \alpha, \beta, \epsilon) = (1e3, 1e5, 1e7, 2e{-}2)$ (high stiffness case).

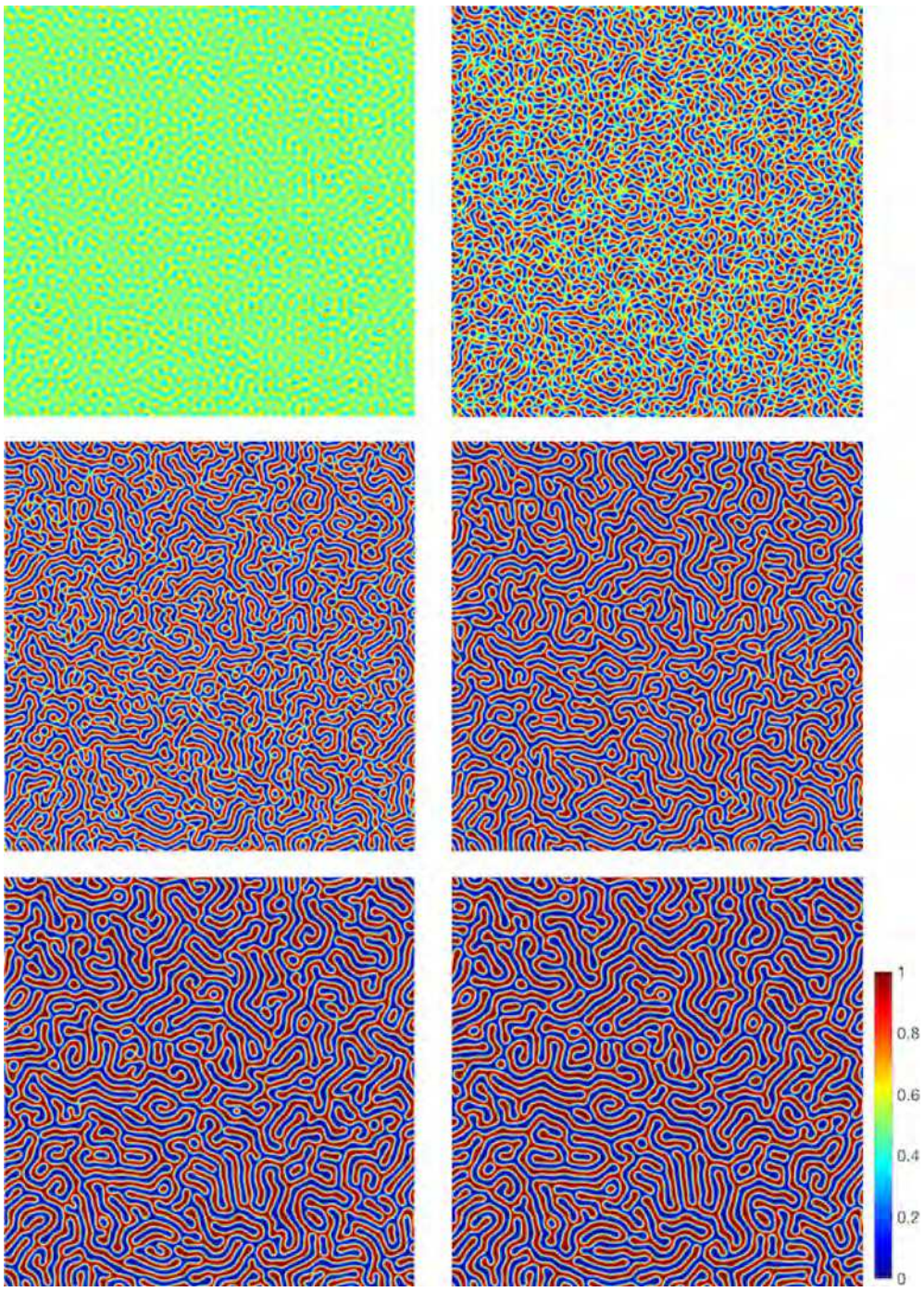

Fig. 4.4. The 2D dynamical evolution of the local volume fraction phase variable ϕ with the initial condition $\hat{\phi}_0 = 0.5$, the time step $\delta t = 0.01$, and model parameters (4.3). Snapshots of the numerical approximation are taken at $t = 60$, 80, 120, 200, 500, and 1000.

with suitable boundary conditions, where $\phi \in L_0^2(\Omega) := \{\phi \in L^2(\Omega) : \int_\Omega \phi d\boldsymbol{x} = 0\}$. The scalar function $\bar{g}(\phi)$ is defined as

$$\bar{g}(\phi) = \frac{1}{|\Omega|} \int_\Omega g(\phi) d\boldsymbol{x}. \tag{2.3}$$

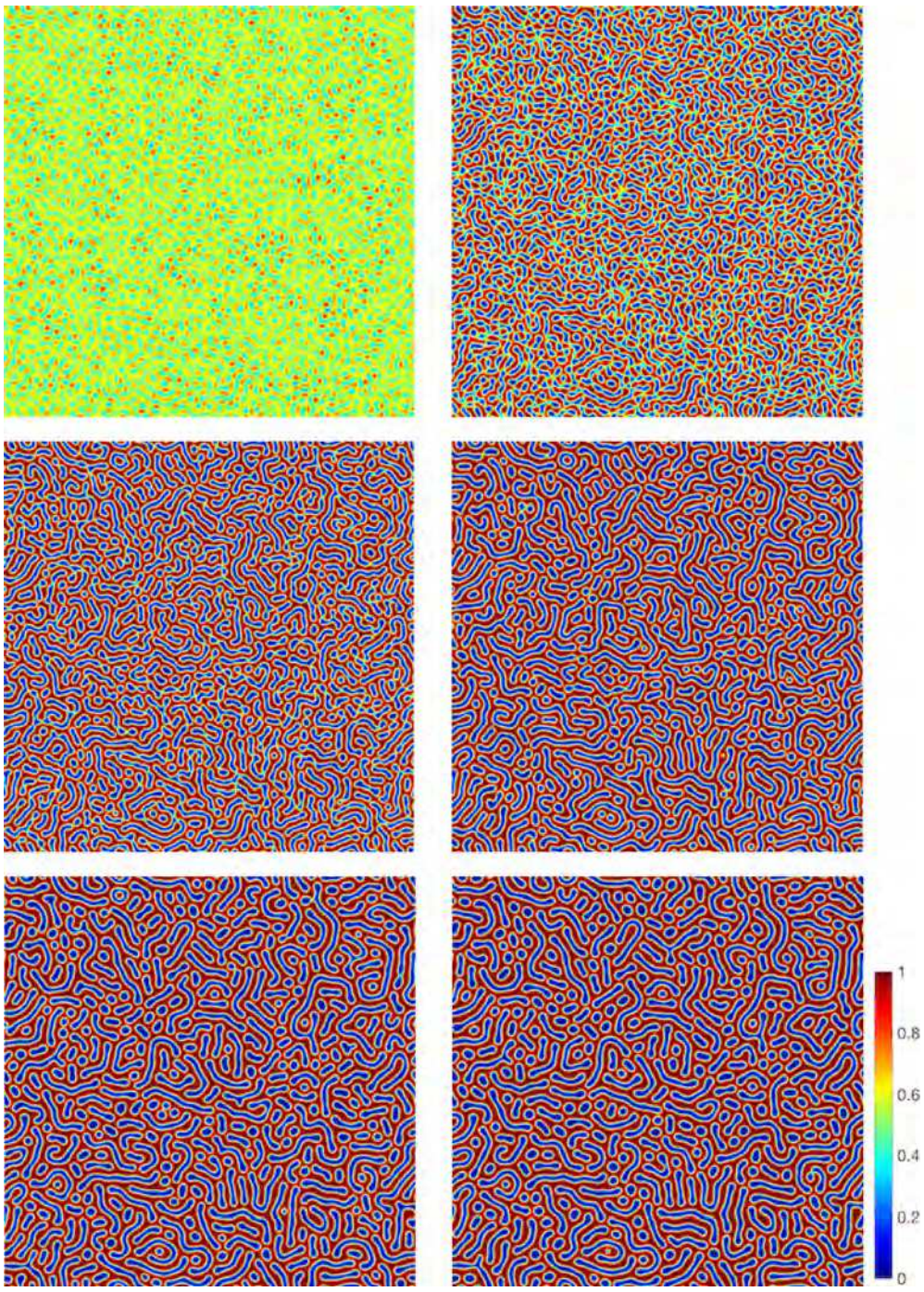

Fig. 4.5. The 2D dynamical evolution of the local volume fraction phase variable ϕ with the initial condition $\hat{\phi}_0 = 0.55$, the time step $\delta t = 0.01$, and model parameters (4.3). Snapshots of the numerical approximation are taken at $t = 60$, 80, 120, 200, 500, and 1000.

The function $g(\phi)$ satisfies the following condition

$$g(0) = 0, g(1) = 1, g'(0) = g'(1) = 0, \tag{2.4}$$

hence in [1], $g(\phi)$ takes the following polynomial form

$$g(\phi) = 6\phi^5 - 15\phi^4 + 10\phi^3. \tag{2.5}$$

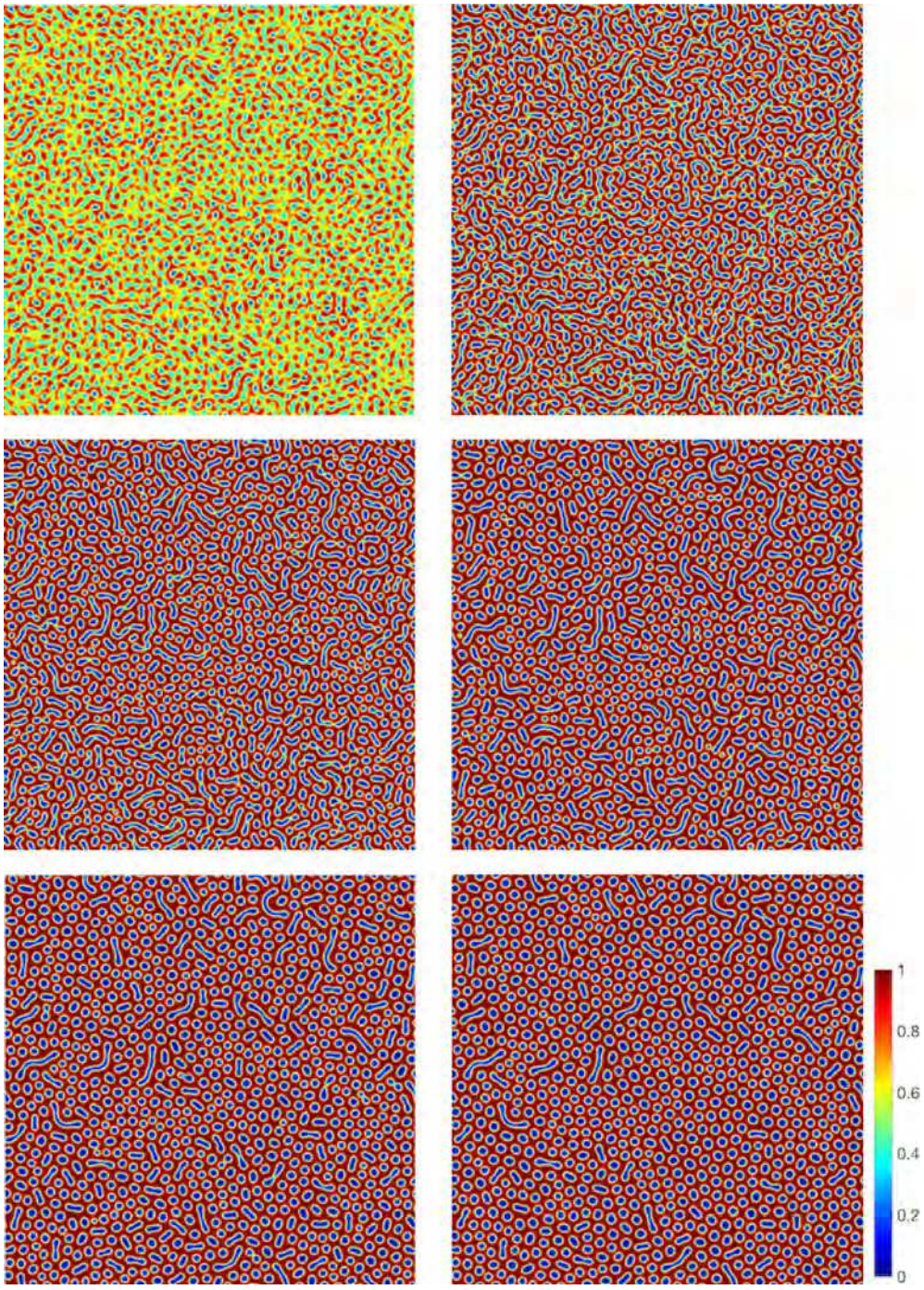

Fig. 4.6. The 2D dynamical evolution of the local volume fraction phase variable ϕ with the initial condition $\hat{\phi}_0 = 0.6$, the time step $\delta t = 0.01$, and model parameters (4.3). Snapshots of the numerical approximation are taken at $t = 60$, 80, 120, 200, 500, and 1000.

For comparison, we remark that the choice $g(\phi) = \phi$ is common in the classical phase-field models for diblock copolymers, cf. [2–8]. About the advantages/disadvantages for these two choices of $g(\phi)$, we refer to [1] for the detailed discussions.

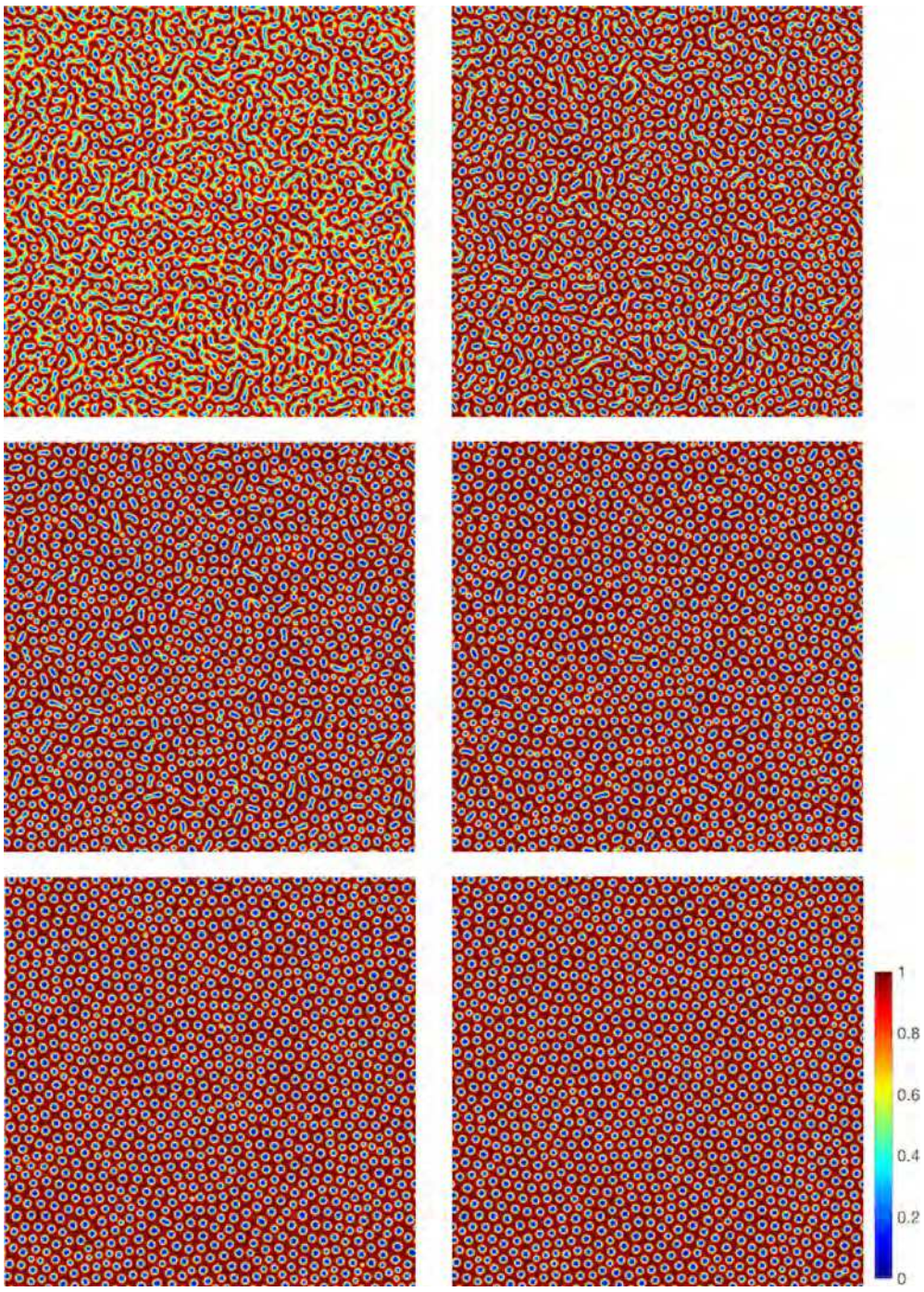

Fig. 4.7. The 2D dynamical evolution of the local volume fraction phase variable ϕ with the initial condition $\hat{\phi}_0 = 0.65$, the time step $\delta t = 0.01$, and model parameters (4.3). Snapshots of the numerical approximation are taken at $t = 60$, 80, 120, 200, 500, and 1000.

Part III is the penalization potential to enforce the "modified" volume conserved approximately, i.e.,

$$\int_{\Omega} g(\phi) d\boldsymbol{x} \approx \int_{\Omega} g(\phi_0) d\boldsymbol{x}, \tag{2.6}$$

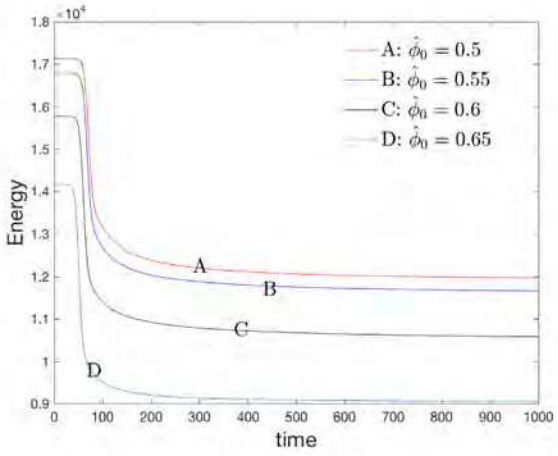

(a) Time evolution of the total free energy.

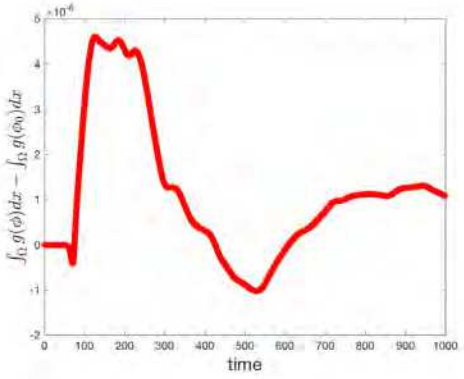

(b) Modified volume difference with $\hat{\phi}_0 = 0.5$.

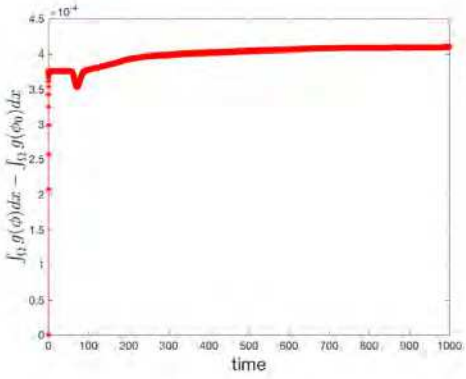

(c) Modified volume difference with $\hat{\phi}_0 = 0.55$.

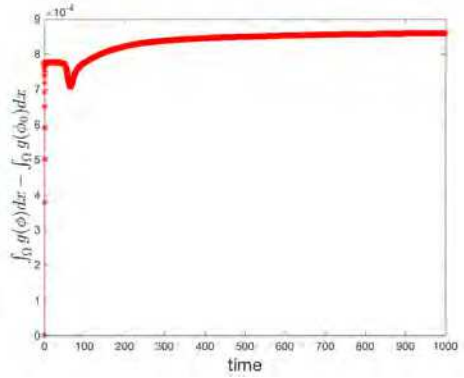

(d) Modified volume difference with $\hat{\phi}_0 = 0.6$.

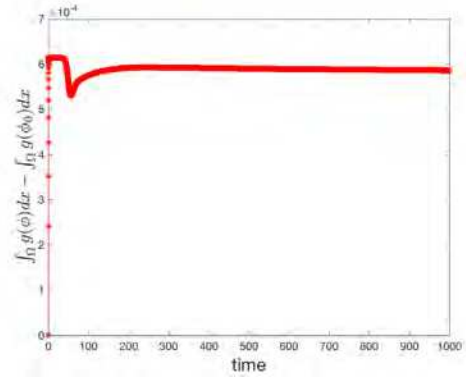

(e) Modified volume difference with $\hat{\phi}_0 = 0.65$.

Fig. 4.8. (a) Time evolution of the free energy functional (3.3) for the 2D spinodal decomposition example with the initial values of $\hat{\phi}_0 = 0.5$, 0.55, 0.6, and 0.65; (b)–(e) Time evolution of the modified volume difference $\int_\Omega g(\phi)d\boldsymbol{x} - \int_\Omega g(\phi_0)d\boldsymbol{x}$.

where ϕ_0 is the initial condition and the parameter is set as $\beta \gg 1$. When $g(\phi) = \phi$, the modified volume degenerates to the real volume. The similar penalization approach had been widely used in Allen–Cahn type equations with some constraints, for example, the liquid crystal models with unit length constraint [33,34], and phase-field elastic bending models for vesicle membranes with conserved volume constraint [35], etc.

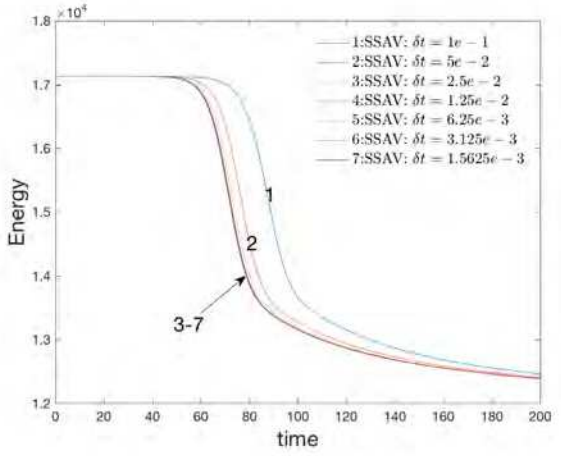

(a) SSAV.

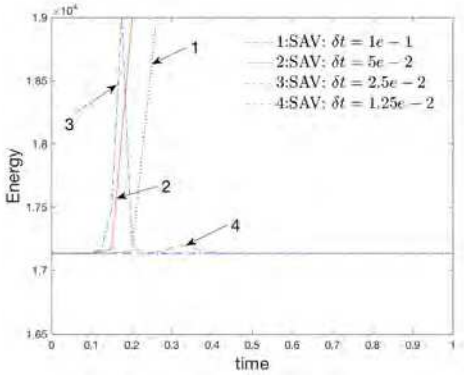

(b) SAV with large time steps.

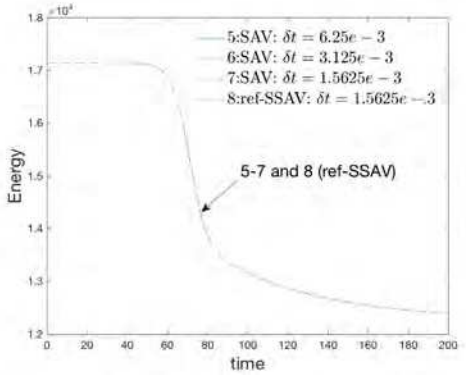

(c) SAV with small time steps.

Fig. 4.9. Time evolutions of the total free energy (3.3) computed by seven different time step sizes until $t = 200$ using the two schemes SSAV and SAV.

The phenomenological mesoscopic dynamic equation that relates a temporal change of $\phi(\boldsymbol{x}, t)$ is governed by the following Allen–Cahn equation (cf. [14,15,36,37]):

$$\frac{1}{M}\phi_t + \frac{\delta E(\phi)}{\delta \phi} = 0, \tag{2.7}$$

where M is the mobility parameter and $\frac{\delta E(\phi)}{\delta \phi}$ is the variational derivative. By taking the total free energy described in (2.1), the PDE system (2.7) turns into

$$\frac{1}{M}\phi_t - \epsilon^2 \Delta\phi + f(\phi) + \alpha\epsilon^2 \psi g'(\phi) + \beta\epsilon^2 \Big(\int_\Omega g(\phi) d\boldsymbol{x} - \int_\Omega g(\phi_0) d\boldsymbol{x}\Big) g'(\phi) = 0, \tag{2.8}$$

$$\psi = (-\Delta)^{-1}(g(\phi) - \bar{g}(\phi)), \tag{2.9}$$

where $f(\phi) = F'(\phi)$. Without loss of generality, we adopt the periodic boundary condition to remove all complexities associated with the boundary integrals in this study. We remark that the boundary conditions can also be the no-flux type as

$$\partial_{\mathbf{n}}\phi|_{\partial\Omega} = \partial_{\mathbf{n}}\psi|_{\partial\Omega} = 0, \tag{2.10}$$

where $\mathbf{n}$ is the outward normal of the computational domain Ω. All numerical analysis in this paper can be carried out to the no-flux boundary conditions without any further difficulties.

The model (2.8)–(2.9) follows the energy dissipation law. By taking the L^2 inner product of (2.8) with ϕ_t, performing integration by parts, we obtain

$$\begin{aligned}&\frac{d}{dt}\left(\int_\Omega(\frac{\epsilon^2}{2}|\nabla\phi|^2+F(\phi))d\boldsymbol{x}+\frac{\beta\epsilon^2}{2}\left(\int_\Omega g(\phi)d\boldsymbol{x}-\int_\Omega g(\phi_0)d\boldsymbol{x}\right)^2\right)+\alpha\epsilon^2(\psi g'(\phi),\phi_t)\\&=-\frac{1}{M}\|\phi_t\|^2.\end{aligned}\tag{2.11}$$

We rewrite (2.9) as

$$\begin{cases}\Delta\psi=g(\phi)-\bar{g}(\phi),\\\int_\Omega\psi d\boldsymbol{x}=0,\end{cases}\tag{2.12}$$

and then take the time derivative for the first equation of (2.12) to obtain

$$-\Delta\psi_t=g'(\phi)\phi_t-\frac{1}{|\Omega|}\int_\Omega g'(\phi)\phi_t d\boldsymbol{x}.\tag{2.13}$$

By taking the L^2 inner product of the above equation with $\alpha\epsilon^2\psi$, we obtain

$$\frac{d}{dt}\int_\Omega\frac{\alpha\epsilon^2}{2}|\nabla\psi|^2d\boldsymbol{x}=\alpha\epsilon^2(g'(\phi)\phi_t,\psi),\tag{2.14}$$

where the zero mean property of ψ is used. By combining (2.11) and (2.14), we obtain

$$\frac{d}{dt}E(\phi,\psi)=-\frac{1}{M}\|\phi_t\|^2,\tag{2.15}$$

where

$$E(\phi,\psi)=\int_\Omega(\frac{\epsilon^2}{2}|\nabla\phi|^2+F(\phi)+\frac{\alpha\epsilon^2}{2}|\nabla\psi|^2)d\boldsymbol{x}+\frac{\beta\epsilon^2}{2}\left(\int_\Omega g(\phi)d\boldsymbol{x}-\int_\Omega g(\phi_0)d\boldsymbol{x}\right)^2.\tag{2.16}$$

3. Numerical schemes

We develop a second-order accurate and provably unconditionally energy stable scheme by combining the SAV approach [28] with the stabilization technique, that arrives at the stabilized-SAV approach. An extra linear stabilization term is particularly efficient to enhance the energy stability while keeping the computation fast with the required accuracy.

We define a scalar, auxiliary variable $u(t)$ as follows:

$$u(t)=\sqrt{\int_\Omega F(\phi)d\boldsymbol{x}+G(\phi)+B},\tag{3.1}$$

where

$$G(\phi)=\int_\Omega\frac{\alpha\epsilon^2}{2}|\nabla(-\Delta)^{-1}(g(\phi)-\bar{g}(\phi))|^2d\boldsymbol{x}+\frac{\beta\epsilon^2}{2}\left(\int_\Omega g(\phi)d\boldsymbol{x}-\int_\Omega g(\phi_0)d\boldsymbol{x}\right)^2\tag{3.2}$$

where B is any constant that ensures the radicand positive (in all numerical examples, we let $B=1$). Thus the total free energy (2.16) can be rewritten as

$$E(u,\phi)=\int_\Omega\frac{\epsilon^2}{2}|\nabla\phi|^2d\boldsymbol{x}+u^2-B.\tag{3.3}$$

By taking the time derivative for the new variable $u(t)$, we can rewrite the system (2.8)–(2.9) to be the following system in terms of ϕ and u,

$$\frac{1}{M}\phi_t-\epsilon^2\Delta\phi+uH=0,\tag{3.4}$$

$$u_t=\frac{1}{2}\int_\Omega H(\phi)\phi_t d\boldsymbol{x},\tag{3.5}$$

where

$$H(\phi)=\frac{f(\phi)+\alpha\epsilon^2\big((-\Delta)^{-1}(g(\phi)-\bar{g}(\phi))\big)g'(\phi)+\beta\epsilon^2(\int_\Omega g(\phi)d\boldsymbol{x}-\int_\Omega g(\phi_0)d\boldsymbol{x})g'(\phi)}{\sqrt{\int_\Omega F(\phi)d\boldsymbol{x}+G(\phi)+B}}.\tag{3.6}$$

The transformed system (3.4)–(3.5) forms a closed PDE system with the following initial conditions,

$$\begin{cases} \phi(t=0)=\phi_0, \\ u(t=0)=\sqrt{\int_\Omega F(\phi_0)d\boldsymbol{x}+G(\phi_0)+B}. \end{cases} \tag{3.7}$$

The system (3.4)–(3.5) also preserves the energy dissipative law. By taking the L^2 inner product of (3.4) with ϕ_t, and multiplying (3.5) with $2u$, performing integration by parts, and summing two obtained equalities up, we can obtain the energy dissipation law as

$$\frac{d}{dt}E(u,\phi)=-\frac{1}{M}\|\phi_t\|^2\le 0. \tag{3.8}$$

Let $\delta t>0$ be a time step size and set $t^n=n\delta t$ for $0\le n\le N$ with $T=N\delta t$. We also denote the L^2 inner product of any two spatial functions $\phi(\boldsymbol{x})$ and $\psi(\boldsymbol{x})$ by $(\phi(\boldsymbol{x}),\psi(\boldsymbol{x}))=\int_\Omega\phi(\boldsymbol{x})\psi(\boldsymbol{x})d\boldsymbol{x}$, and the L^2 norm of the function $\phi(\boldsymbol{x})$ by $\|\phi\|^2=(\phi,\phi)$. Let ψ^n denotes the numerical approximation to $\psi(\cdot,t)|_{t=t^n}$ for any function ψ.

We now construct a numerical scheme based on the second-order backward differentiation formula (BDF2) for solving the system (3.4)–(3.5), that reads as follows.

Assuming ϕ^n, u^n and ϕ^{n-1}, u^{n-1} are known, we update ϕ^{n+1}, u^{n+1} by solving

$$\frac{3\phi^{n+1}-4\phi^n+\phi^{n-1}}{2M\delta t}-\epsilon^2\Delta\phi^{n+1}+u^{n+1}H^{*,n+1}+S(\phi^{n+1}-\phi^{*,n+1})=0, \tag{3.9}$$

$$3u^{n+1}-4u^n+u^{n-1}=\frac{1}{2}\int_\Omega H^{*,n+1}(3\phi^{n+1}-4\phi^n+\phi^{n-1})d\boldsymbol{x}, \tag{3.10}$$

where

$$\phi^{*,n+1}=2\phi^n-\phi^{n-1},\ H^{*,n+1}=H(\phi^{*,n+1}), \tag{3.11}$$

and S is a positive stabilizing parameter.

Remark 3.1. In (3.9), an extra second-order linear stabilizer (associated with S) is added in the scheme. The error that this term introduces is of the order $S\delta t^2\phi_{tt}(\cdot)$ that is of the same order as the error introduced by the second-order extrapolation of the nonlinear term $f(\phi)$. Numerical simulations show that as long as $S\sim\|f(\phi)\|_{L^\infty}$, the scheme can get better accuracy and stability result. This stabilizer term is crucial to enhance the stability while keeping the required accuracy, cf. the comparison with the non-stabilized SAV scheme in Figs. 4.2, 4.3 and 4.9.

Remark 3.2. To initiate the second-order scheme (3.9)–(3.10), we need the values of ϕ^1, u^1, that can be obtained by the following similar first-order scheme based on backward Euler formulation that reads as,

$$\frac{\phi^1-\phi^0}{M\delta t}-\epsilon^2\Delta\phi^1+u^1H^0+S(\phi^1-\phi^0)=0, \tag{3.12}$$

$$u^1-u^0=\frac{1}{2}\int_\Omega H^0(\phi^1-\phi^0)d\boldsymbol{x}, \tag{3.13}$$

where $H^0=H(\phi^0)$, $\phi^0=\phi_0$.

Apparently, one has to solve a linear but nonlocal and coupled system for ϕ^{n+1} and u^{n+1} in the scheme (3.9)–(3.10) that might need costly iterative solvers. But in practice, we can implement the scheme through the following decoupling procedure.

We first rewrite (3.10) as follows,

$$u^{n+1}=\frac{1}{2}\int_\Omega H^{*,n+1}\phi^{n+1}d\boldsymbol{x}+r^n, \tag{3.14}$$

where

$$r^n=\frac{4u^n-u^{n-1}}{3}-\frac{1}{2}\int_\Omega H^{*,n+1}\frac{4\phi^n-\phi^{n-1}}{3}d\boldsymbol{x}. \tag{3.15}$$

Then the scheme (3.9)–(3.10) can be combined together to be

$$(\frac{3}{2M\delta t}+S)\phi^{n+1}-\epsilon^2\Delta\phi^{n+1}+\frac{1}{2}H^{*,n+1}\int_\Omega H^{*,n+1}\phi^{n+1}d\boldsymbol{x}=\tilde{r}^n, \tag{3.16}$$

where $\tilde{r}^n$ is an explicit term defined as

$$\tilde{r}^n=\frac{4\phi^n-\phi^{n-1}}{2M\delta t}+S\phi^{*,n+1}-r^nH^{*,n+1}. \tag{3.17}$$

Thus (3.16) can be written as

$$\mathscr{P}(\phi^{n+1}) + \frac{1}{2}H^{*,n+1}\int_{\Omega} H^{*,n+1}\phi^{n+1}d\boldsymbol{x} = \tilde{r}^n, \tag{3.18}$$

where $\mathscr{P}(\cdot)$ is the linear operator that is defined as

$$\mathscr{P}(\psi) = (\frac{3}{2M\delta t} + S - \epsilon^2\Delta)\psi. \tag{3.19}$$

Define a linear operator $\mathscr{P}^{-1}(\cdot)$, such that for any periodic function $\phi \in L^2(\Omega)$, $\psi = \mathscr{P}^{-1}(\phi)$ is the solution of the following linear system

$$\mathscr{P}(\psi) = \phi, \tag{3.20}$$

with periodic boundary conditions. By applying the operator $\mathscr{P}^{-1}$ to (3.18), then we obtain

$$\phi^{n+1} + \frac{1}{2}\mathscr{P}^{-1}(H^{*,n+1})\int_{\Omega} H^{*,n+1}\phi^{n+1}d\boldsymbol{x} = \mathscr{P}^{-1}(\tilde{r}^n). \tag{3.21}$$

By taking the L^2 inner product of (3.21) with $H^{*,n+1}$, we obtain

$$\int_{\Omega} H^{*,n+1}\phi^{n+1}d\boldsymbol{x} = \frac{\int_{\Omega} H^{*,n+1}\mathscr{P}^{-1}(\tilde{r}^n)d\boldsymbol{x}}{1 + \frac{1}{2}\int_{\Omega} H^{*,n+1}\mathscr{P}^{-1}(H^{*,n+1})d\boldsymbol{x}}. \tag{3.22}$$

It is easy to check the term in the denominator $\int_{\Omega} H^{*,n+1}\mathscr{P}^{-1}(H^{*,n+1})d\boldsymbol{x} \geq 0$ since $\mathscr{P}^{-1}$ is a positive definite operator, that implies the explicit formula (3.22) is uniquely solvable.

Furthermore, (3.22) actually provides an explicit formulation for the nonlocal term $\int_{\Omega} H^{*,n+1}\phi^{n+1}d\boldsymbol{x}$. Therefore, in computations, we first find $\psi_1 = \mathscr{P}^{-1}(\tilde{r}^n)$ and $\psi_2 = \mathscr{P}^{-1}(H^{*,n+1})$, that means to solve the following two decoupled elliptic equations,

$$(\frac{3}{2M\delta t} + S - \epsilon^2\Delta)\psi_1 = \tilde{r}^n, \tag{3.23}$$

and

$$(\frac{3}{2M\delta t} + S - \epsilon^2\Delta)\psi_2 = H^{*,n+1}, \tag{3.24}$$

with the periodic boundary conditions. And then, after by applying (3.22) to update $\int_{\Omega} H^{*,n+1}\phi^{n+1}d\boldsymbol{x}$, we can obtain ϕ^{n+1} from (3.21) directly.

To summarize, the nonlocal coupled scheme (3.9)–(3.10) can be easily implemented in the following manner:

- Compute ψ_1 and ψ_2 by solving two linear elliptic equations with constant coefficients, (3.23) and (3.24);
- Compute $\int_{\Omega} H^{*,n+1}\phi^{n+1}d\boldsymbol{x}$ from (3.22) and update u^{n+1} from (3.14);
- Update ϕ^{n+1} from (3.21).

Hence, the total cost at each time step is essentially *solving two decoupled elliptic equations* in the above process and *one elliptic equation* in the computations of $G(\phi)$ in (3.2). All elliptic equations are equipped with the constant coefficients. We note that these equations with periodic boundary conditions can be easily computed by the Fourier-Spectral method. Hence, this scheme is extremely efficient and easy to implement.

Now we prove the scheme (3.9)–(3.10) is unconditionally energy stable as follows.

Theorem 3.1. *The scheme (3.9)–(3.10) is unconditionally energy stable which satisfies the following discrete energy dissipation law,*

$$\frac{1}{\delta t}(E^{n+1} - E^n) \leq -\frac{1}{M}\|\frac{3\phi^{n+1} - 4\phi^n + \phi^{n-1}}{2\delta t}\|^2 \leq 0, \tag{3.25}$$

where

$$\begin{aligned} E^{n+1} = {} & \frac{\epsilon^2}{2}(\frac{\|\nabla\phi^{n+1}\|^2 + \|2\nabla\phi^{n+1} - \nabla\phi^n\|^2}{2}) + \frac{(u^{n+1})^2 + (2u^{n+1} - u^n)^2}{2} \\ & + S\frac{\|\phi^{n+1} - \phi^n\|^2}{2}. \end{aligned} \tag{3.26}$$

Proof. By taking the L^2 inner product of (3.9) with $3\phi^{n+1} - 4\phi^n + \phi^{n-1}$, and using integration by parts, we obtain

$$\begin{aligned} \frac{1}{2M\delta t}\|3\phi^{n+1} - 4\phi^n + \phi^{n-1}\|^2 & + \epsilon^2(\nabla\phi^{n+1}, 3\nabla\phi^{n+1} - 4\nabla\phi^n + \nabla\phi^{n-1}) \\ & + u^{n+1}(H^{*,n+1}, 3\phi^{n+1} - 4\phi^n + \phi^{n-1}) \\ & + S(\phi^{n+1} - 2\phi^n + \phi^{n-1}, 3\phi^{n+1} - 4\phi^n + \phi^{n-1}) = 0 \end{aligned} \tag{3.27}$$

By multiplying (3.10) with $2u^{n+1}$, we obtain

$$2(3u^{n+1}-4u^n+u^{n-1})u^{n+1}=u^{n+1}\int_\Omega H^{*,n+1}(3\phi^{n+1}-4\phi^n+\phi^{n-1})d\boldsymbol{x}. \tag{3.28}$$

Combining the above equations and applying the following two identities

$$\begin{aligned}&2a(3a-4b+c)=a^2+(2a-b)^2-b^2-(2b-c)^2+(a-2b+c)^2,\\&(3a-4b+c)(a-2b+c)=(a-b)^2-(b-c)^2+2(a-2b+c)^2,\end{aligned} \tag{3.29}$$

we obtain

$$\begin{aligned}&\frac{\epsilon^2}{2}(\|\nabla\phi^{n+1}\|^2+\|2\nabla\phi^{n+1}-\nabla\phi^n\|^2)-\frac{\epsilon^2}{2}(\|\nabla\phi^n\|^2+\|2\nabla\phi^n-\nabla\phi^{n-1}\|^2)\\&+\left((u^{n+1})^2+(2u^{n+1}-u^n)^2\right)-\left((u^n)^2+(2u^n-u^{n-1})^2\right)\\&+S\|\phi^{n+1}-\phi^n\|^2-S\|\phi^n-\phi^{n-1}\|^2\\&+\frac{\epsilon^2}{2}\|\nabla\phi^{n+1}-2\nabla\phi^n+\nabla\phi^{n-1}\|^2+(u^{n+1}-2u^n+u^{n-1})^2\\&+2S\|\phi^{n+1}-2\phi^n+\phi^{n-1}\|^2=-\frac{1}{2M\delta t}\|3\phi^{n+1}-4\phi^n+\phi^{n-1}\|^2.\end{aligned}$$

Finally, we obtain the desired result after dropping some positive terms. □

Remark 3.3. Heuristically, $\frac{1}{\delta t}(E^{n+1}-E^n)$ is a second-order approximation of $\frac{d}{dt}E(u,\phi)$ at $t=t^{n+1}$. For any smooth variable ψ with time, we have

$$\begin{aligned}&\frac{\|\psi^{n+1}\|^2-\|2\psi^{n+1}-\psi^n\|^2}{2\delta t}-\frac{\|\psi^n\|^2-\|2\psi^n-\psi^{n-1}\|^2}{2\delta t}\\&\cong\frac{\|\psi^{n+2}\|^2-\|\psi^n\|^2}{2\delta t}+O(\delta t^2)\cong\frac{d}{dt}\|\psi(t^{n+1})\|^2+O(\delta t^2),\end{aligned} \tag{3.30}$$

and

$$\frac{\|\psi^{n+1}-\psi^n\|^2-\|\psi^n-\psi^{n-1}\|^2}{2\delta t}\cong O(\delta t^2). \tag{3.31}$$

Remark 3.4. Although we consider only time discrete schemes in this study, the results can be carried over to any consistent finite-dimensional Galerkin approximations in the space since the proofs are all based on a variational formulation with all test functions in the same space as the space of the trial functions.

Remark 3.5. In comparison with the stabilized SAV scheme developed above, we also present the first-order linear stabilized explicit scheme that was developed in [1], where the nonlinear terms are treated in an explicit way and some stabilizers are added to enhance the stability. About the detailed proof of its unconditional energy stability, we refer to [1]. The first-order linear stabilized explicit scheme reads as follows.

$$\begin{aligned}&\frac{\phi^{n+1}-\phi^n}{M\delta t}-\epsilon^2\Delta\phi^{n+1}+S(\phi^{n+1}-\phi^n)+\alpha\epsilon^2(-\Delta)^{-1}(\phi^{n+1}-\phi^n)\\&=-f(\phi^n)-\alpha\epsilon^2((-\Delta)^{-1}(g(\phi^n)-\bar{g}(\phi^n)))g'(\phi^n)\\&\quad-\beta\epsilon^2\int_\Omega g(\phi^n)d\boldsymbol{x}-\int_\Omega g(\phi_0)d\boldsymbol{x}g'(\phi^n).\end{aligned} \tag{3.32}$$

4. Numerical simulations

In this section, we present numerous 2D and 3D numerical examples to demonstrate the accuracy and energy stability the developed stabilized-SAV scheme (3.9)–(3.10). In all examples, we consider a computational domain $\Omega=[0,2\pi]^d$, $d=2,3$ with periodic boundary conditions and we adopt the Fourier-spectral method to discretize the space.

4.1. Accuracy tests

We perform numerical simulations to test the convergence rates of the proposed stabilized-SAV scheme (3.9)–(3.10), denoted by SSAV for short. For comparison, we also compute the convergence rates by using the non-stabilized version of SAV scheme, i.e., scheme (3.9)–(3.10) but with $S=0$, denoted by SAV for short, and the first-order linear stabilized explicit scheme (3.32), denoted by SExpl-1st for short.

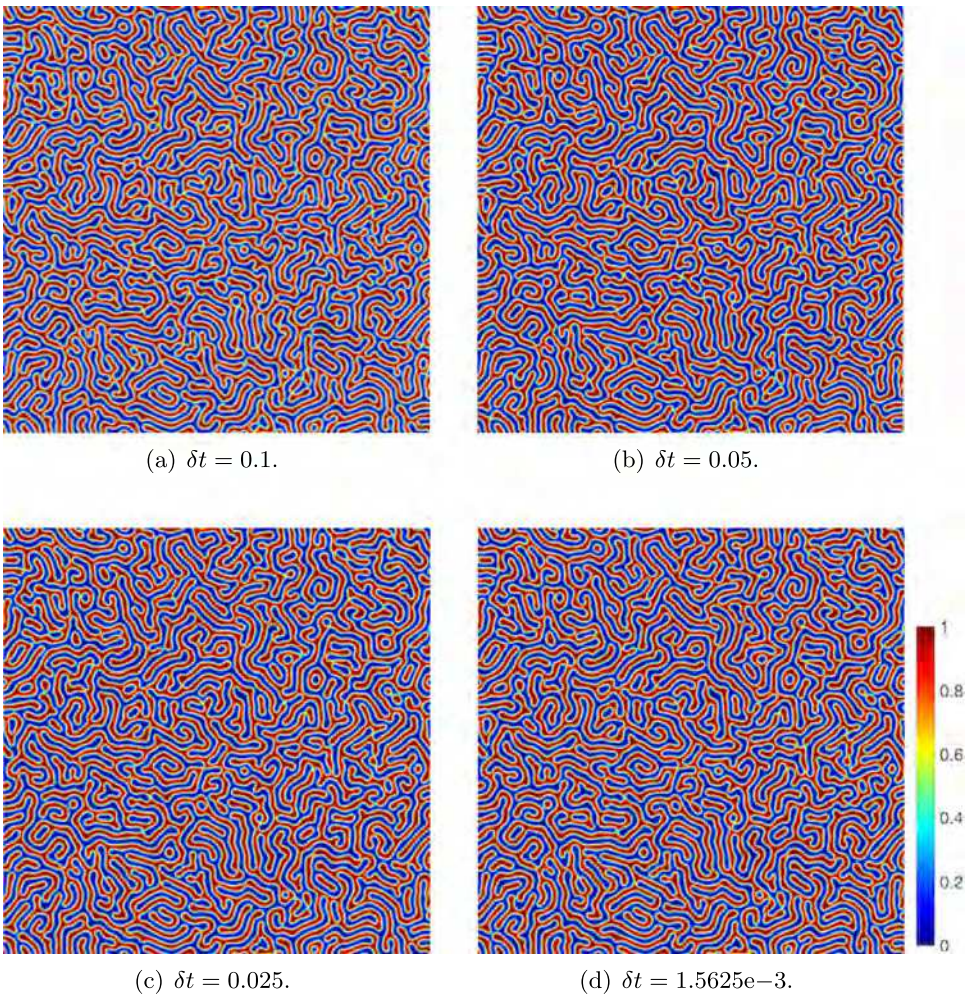

(a) $\delta t = 0.1$. (b) $\delta t = 0.05$.

(c) $\delta t = 0.025$. (d) $\delta t = 1.5625\text{e}{-3}$.

Fig. 4.10. Qualitative comparison of numerical simulations at $t = 200$ computed by using the scheme SSAV with four different time steps.

We perform refinement tests for temporal convergence by setting the initial condition of a circle as follows,

$$\phi(x, y, t = 0) = -\frac{1}{2}\tanh\left(\frac{\sqrt{(x-\pi)^2 + (y-\pi)^2} - 1.5}{2.5\epsilon}\right) + \frac{1}{2}. \tag{4.1}$$

We set the values of parameters as $S = 2$, $B = 1$ and vary the other four model parameters $(M, \alpha, \beta, \epsilon)$.

Since the exact solution is not known, we choose the solution obtained with the time step size $\delta t = 1\text{e}{-9}$ computed by the scheme SSAV as the benchmark solution (approximately the exact solution) for computing errors. We discretize the 2D domain $\Omega = [0, 2\pi]^2$ by using $N_x = N_y = 129$ Fourier modes for x and y directions so that the errors from the spatial discretization are negligible compared to the temporal discretization errors. The L^2 errors of the phase variable between the numerical solution and the exact solution at $t = 10$ with different time step sizes are then plotted.

We first test the convergence rates for the low stiffness case, where we use $(M, \alpha, \beta, \epsilon) = (1, 1\text{e}{-2}, 1\text{e}{-2}, 6\text{e}{-2})$ that corresponds to small mobility, small nonlocal parameter, small penalization parameter, and large interfacial width parameter. The L^2 errors computed by three schemes SSAV, SAV, and SExpl-1st are shown in Fig. 4.1. We observe that these three schemes present very good convergence rate that almost perfectly matches their respective orders of accuracy for the time step. This implies the stabilization parameter S is not necessary in the SAV scheme for the low stiffness case.

We further test the convergence rates for the high stiffness case, where we set order parameters as $(M, \alpha, \beta, \epsilon) = (1\text{e}1, 1\text{e}3, 1\text{e}5, 2\text{e}{-2})$ and $(M, \alpha, \beta, \epsilon) = (1\text{e}2, 1\text{e}5, 1\text{e}7, 2\text{e}{-2})$ in Figs. 4.2 and 4.3, respectively. This corresponds to large mobility, large nonlocal parameter, large penalization parameter, and small interfacial width parameter. We note

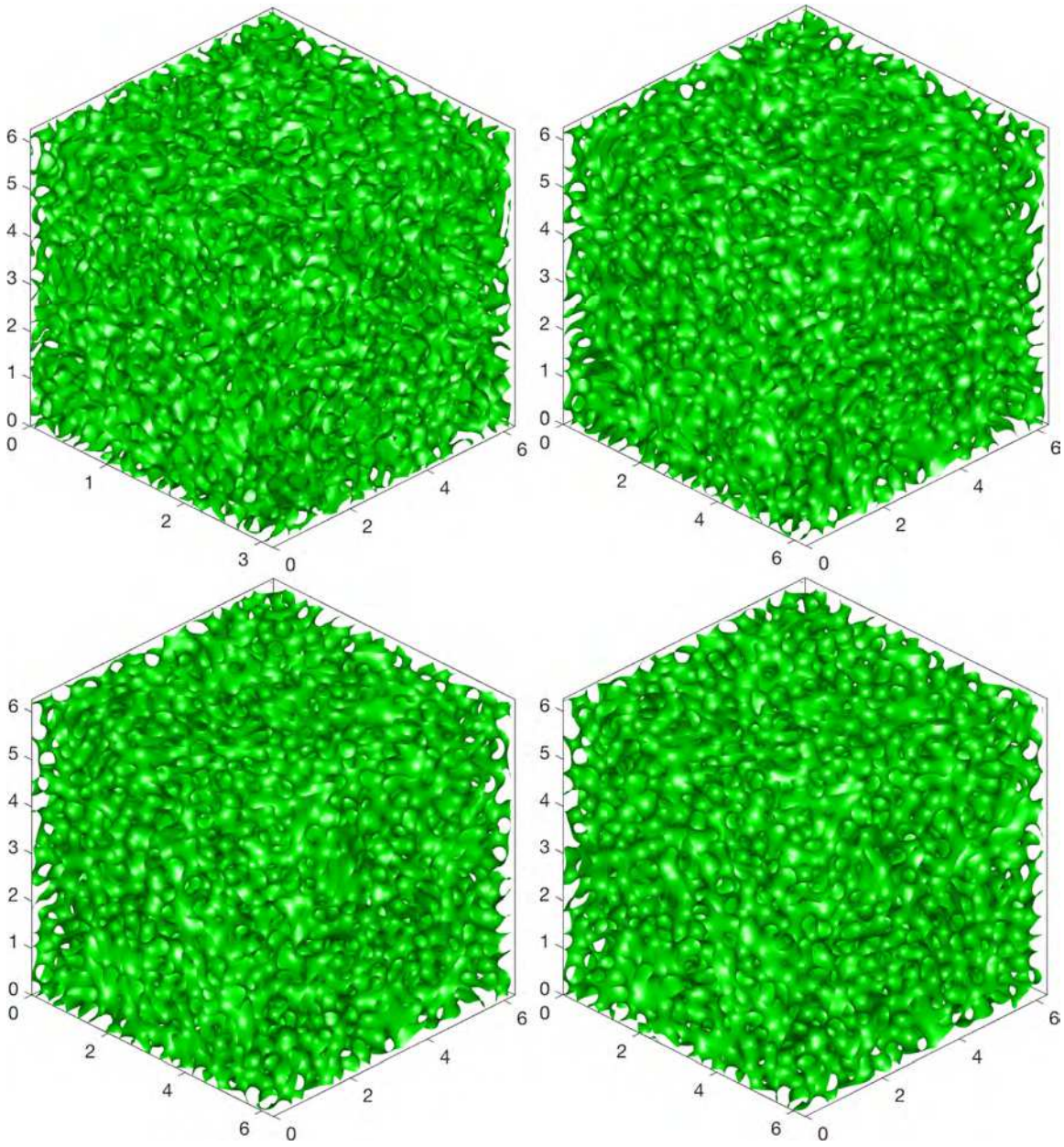

Fig. 4.11. The 3D dynamical evolution of the isosurface of the phase variable ϕ at $t = 80$, 200, 400, and 1000 with the initial condition $\hat{\phi}_0 = 0.5$, time step $\delta t = 0.01$ and model parameter (4.5).

the non-stabilized scheme SAV can only present good approximations and the second-order accuracy for smaller time steps, $\delta t \leq$ 1.5625e−2 shown in Fig. 4.2(a) and $\delta t \leq$ 7.8125e−5 shown in Fig. 4.3(a). On the contrary, the stabilized scheme SSAV and SExpl-1st are stable for all tested time steps and perform good approximations and corresponding orders of accuracy all along. However, the second-order scheme SSAV performs with much better accuracy than that of the first-order scheme SExpl-1st.

Therefore, through these numerical tests, we conclude that (i) if the stiffness is low, both of the stabilized and non-stabilized schemes can solve the model well; (ii) if the stiffness is high, the stabilized scheme SSAV overwhelmingly defeats the non-stabilized scheme from the stability and/or accuracy; (iii) the second-order scheme SSAV presents much better accurate results than the first-order scheme SExpl-1st.

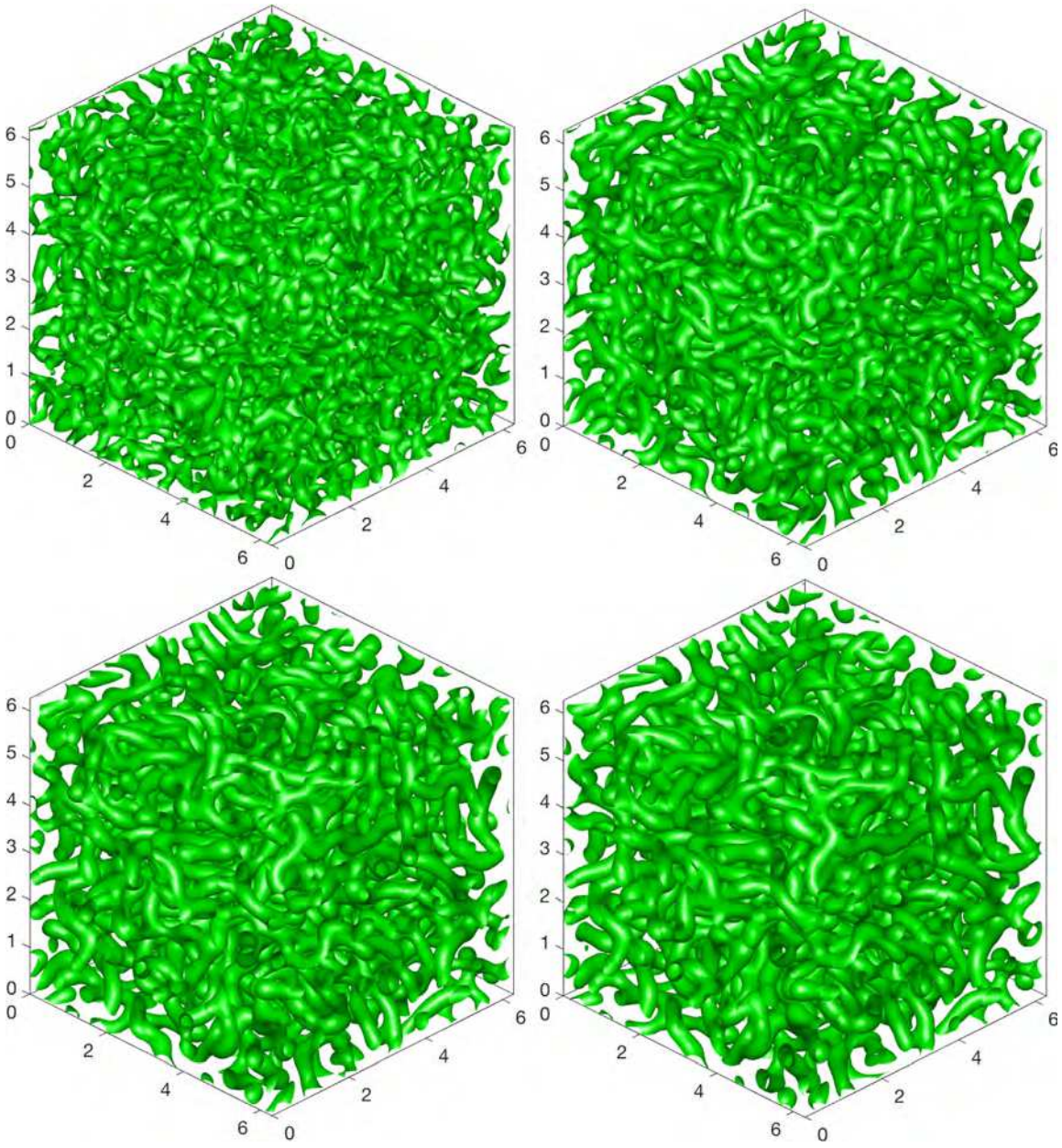

Fig. 4.12. The 3D dynamical evolution of the isosurface of the phase variable ϕ at $t = 80$, 200, 400, and 1000 with the initial condition $\hat{\phi}_0 = 0.65$, time step $\delta t = 0.01$ and model parameter (4.5).

4.2. Spinodal decomposition

In this example, we study the phase separation dynamics that is called spinodal decomposition using the developed scheme SSAV. By considering a homogeneous binary mixture, the spontaneous growth of the concentration fluctuations can lead the system from the homogeneous to the two-phase state.

4.2.1. 2d case

We set the initial condition as the randomly perturbed concentration field as follows,

$$\phi(\boldsymbol{x}, t = 0) = \hat{\phi}_0 + 0.001\text{rand}(\boldsymbol{x}), \tag{4.2}$$

where $\boldsymbol{x} = (x, y)$ and rand$(\boldsymbol{x})$ is the random number in $[-1, 1]$ that follows the normal distribution. We use the stabilized scheme SSAV with the time step $\delta t = 0.01$ and discretize the domain $[0, 2\pi]^2$ using $N_x = N_y = 513$ Fourier modes. Other

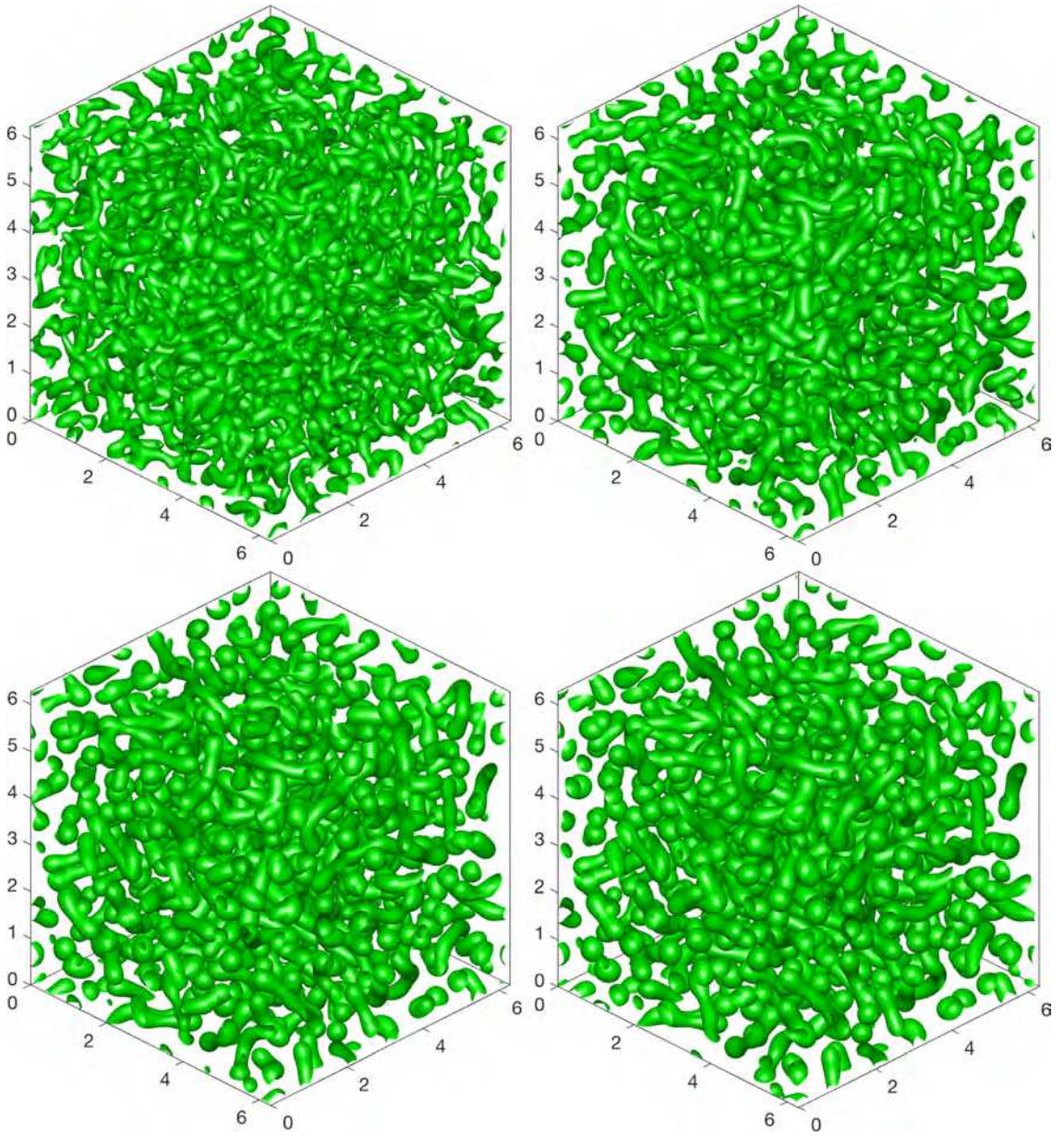

Fig. 4.13. The 3D dynamical evolution of the isosurface of the phase variable ϕ at $t = 80$, 200, 400, and 1000 with the initial condition $\hat{\phi}_0 = 0.7$, time step $\delta t = 0.01$ and model parameter (4.5).

model parameters are set as

$$M = 1, \alpha = 1\text{e}6, \beta = 5\text{e}5, \epsilon = 6\text{e}{-3}, S = 2, B = 1. \tag{4.3}$$

In Fig. 4.4, we perform numerical simulations for the initial value $\hat{\phi}_0 = 0.5$ and snapshots of the phase variable $\phi(\boldsymbol{x}, t)$ are taken at various times. We observe that the blue region is entangled with the red region everywhere and the final equilibrium solution forms the cylindrical phase. In Fig. 4.5, by using $\hat{\phi}_0 = 0.55$, we observe that a small quantity of the blue region starts to form the stacked balls (body-centered-cubic, BCC for short) but most of the blue region still grafts and entangles with the red region. When the initial value is $\hat{\phi}_0 = 0.6$, shown in Fig. 4.6, we observe that more blue regions form the BCC phase and a small quantity of it still forms the cylindrical phase. Finally, by using $\hat{\phi}_0 = 0.65$, shown in Fig. 4.7, we observe that the final equilibrium solution becomes to be the pure BCC phase in the whole domain.

In Fig. 4.8(a), we present the evolution of the total free energy functional (3.3) for all above four cases. The energy curves show the decays with the time that confirms that the scheme SSAV is unconditionally stable. In Fig. 4.8(b), for the

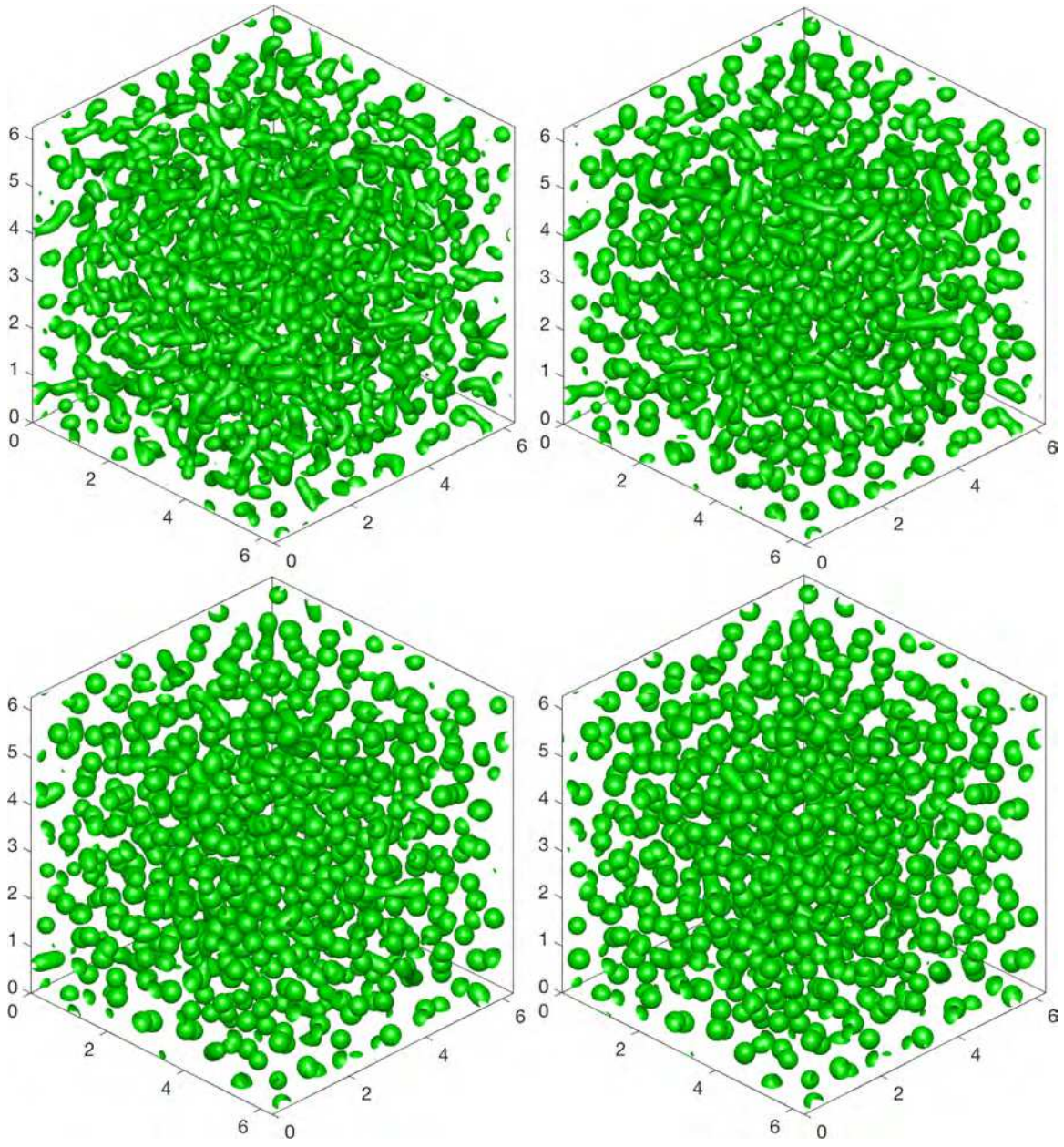

Fig. 4.14. The 3D dynamical evolution of the isosurface of the phase variable ϕ at $t = 80$, 200, 400, and 1000 with the initial condition $\hat{\phi}_0 = 0.75$, time step $\delta t = 0.01$ and model parameter (4.5).

above four cases, we plot the evolutions for the modified volume difference $\int_\Omega g(\phi)d\boldsymbol{x} - \int_\Omega g(\phi_0)d\boldsymbol{x}$ and the magnitude of it for each case is very small.

Finally, we verify whether the stabilized scheme SSAV is unconditionally energy stable for various time steps. We still use the same model parameters and choose $\hat{\phi}_0 = 0.5$. In Fig. 4.9, we plot the evolution curves of the total free energy (3.3) computed by using the two schemes SSAV and SAV. For all tested time steps, the energy curves computed by SSAV show the monotonic decays which confirm that the stabilized algorithm is unconditionally stable, shown in Fig. 4.9(a). On the contrary, when the time step $\delta t > 6.25\text{e}{-3}$, the energies blow up which implies the non-stabilized scheme SAV is not stable for large time steps, shown in Fig. 4.9(b). Only when the time step is small ($\delta t \leq 6.25\text{e}{-3}$) shown in Fig. 4.9(c), the total free energy is computed by SAV decays. In Fig. 4.10, we compare the snapshots of ϕ at $t = 200$ computed by using the stabilized scheme SSAV and four different time steps $\delta t = 0.1$, 0.05, 0.025, and $1.5625\text{e}{-3}$ and no visible difference is noticeable.

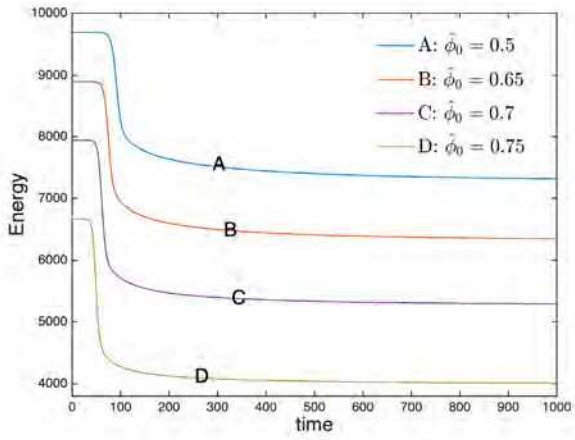

(a) Time evolution of the total free energy.

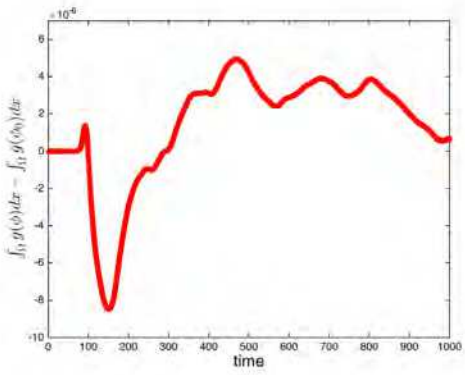

(b) Modified volume difference with $\hat{\phi}_0 = 0.5$.

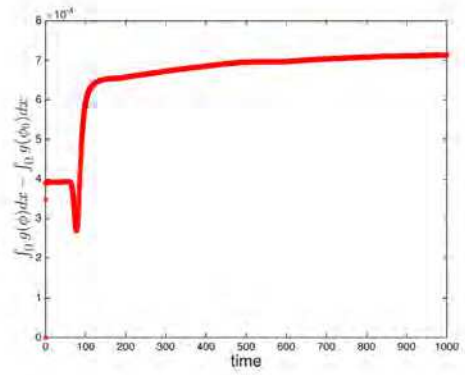

(c) Modified volume difference with $\hat{\phi}_0 = 0.65$.

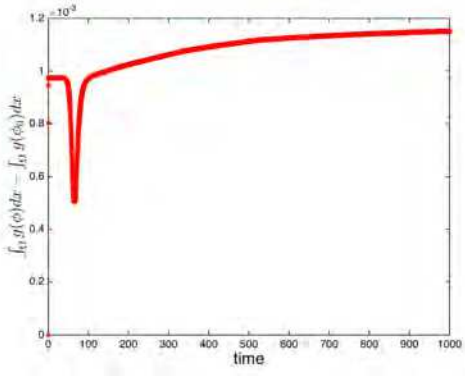

(d) Modified volume difference with $\hat{\phi}_0 = 0.7$.

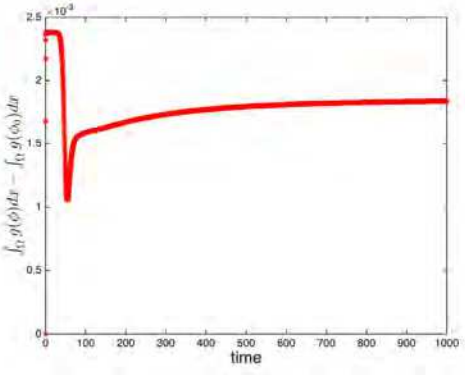

(e) Modified volume difference with $\hat{\phi}_0 = 0.75$.

Fig. 4.15. (a) Time evolution of the free energy functional (3.3) for the 3D spinodal decomposition example with the initial values of $\hat{\phi}_0 = 0.5$, 0.65, 0.7, and 0.75; (b)–(d) Time evolution of the modified volume difference $\int_\Omega g(\phi)d\boldsymbol{x} - \int_\Omega g(\phi_0)d\boldsymbol{x}$ for the four cases.

4.2.2. 3D Case

We further perform the 3D simulations for spinodal decomposition example. We set the initial condition as the randomly perturbed concentration field as follows,

$$\phi(\boldsymbol{x}, t = 0) = \hat{\phi}_0 + 0.001\text{rand}(\boldsymbol{x}), \tag{4.4}$$

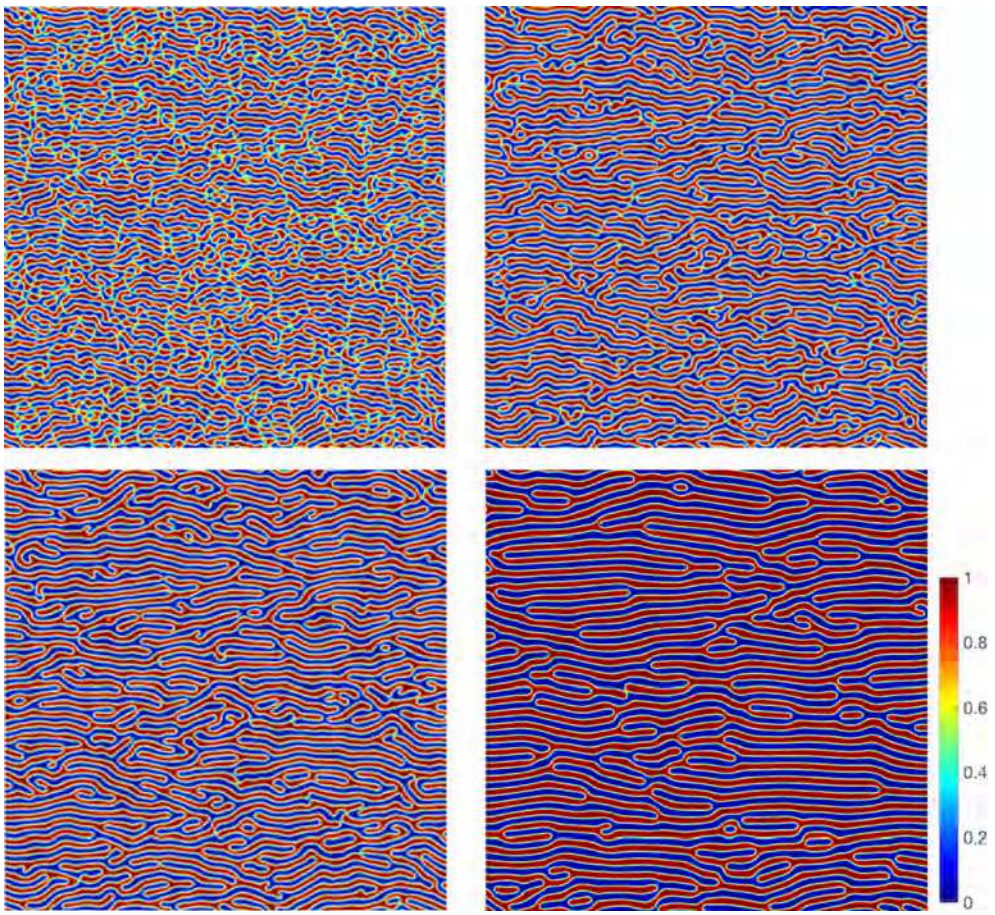

Fig. 4.16. The 2D dynamical evolution of the phase variable ϕ under the imposed electric field where the initial condition $\hat{\phi}_0 = 0.5$, time step $\delta t = 0.01$, and the electric magnitude parameter $\beta = 5e2$. Snapshots of the numerical approximation are taken at $t = 80$, 120, 200, and 2000.

where $\boldsymbol{x} = (x, y, z)$. We use the scheme SSAV with the time step $\delta t = 0.01$ and discretize the space using $N_x = N_y = N_z = 129$ Fourier modes. The computed domain is $[0, 2\pi]^3$ and the parameters are set as

$$M = 1, \alpha = 1e4, \beta = 1e4, \epsilon = 2e{-}2, S = 2, B = 1. \tag{4.5}$$

In Figs. 4.11–4.14, we set the initial value $\hat{\phi}_0 = 0.5$, 0.65, 0.7, and 0.75, respectively. We plot the snapshots of the isosurfaces of $\{\phi(\boldsymbol{x}) = 0.5\}$ at various times. The final equilibrium solution forms the gyroidal (cylindrical) shape for $\hat{\phi}_0 = 0.5$, the mixed gyroidal and spherical shapes for $\hat{\phi}_0 = 0.65$ (dominant cylindrical phase) and $\hat{\phi}_0 = 0.7$ (dominant spherical phase), and the pure spherical phase for $\hat{\phi}_0 = 0.75$. In Fig. 4.15, we present the evolution of the total free energy functional (3.3) and the modified volume difference $\int_\Omega g(\phi)d\boldsymbol{x} - \int_\Omega g(\phi_0)d\boldsymbol{x}$ for these four 3D simulations.

4.3. The imposed electric field

The application of electric fields is an efficient approach to produce various patterns of nano-structured materials. When an external electric field is applied along some direction, an additional term contributed by the electric field is added to the model system (2.8) which reads as follows,

$$\begin{aligned} &\frac{1}{M}\phi_t - \epsilon^2 \Delta\phi \ + f(\phi) + \alpha\epsilon^2 \psi g'(\phi) \\ &\qquad + \beta\epsilon^2 \Big(\int_\Omega g(\phi) d\boldsymbol{x} - \int_\Omega g(\phi_0) d\boldsymbol{x} \Big) g'(\phi) + \gamma\epsilon^2 (-\Delta)^{-1} \phi_{xx} = 0. \end{aligned} \tag{4.6}$$

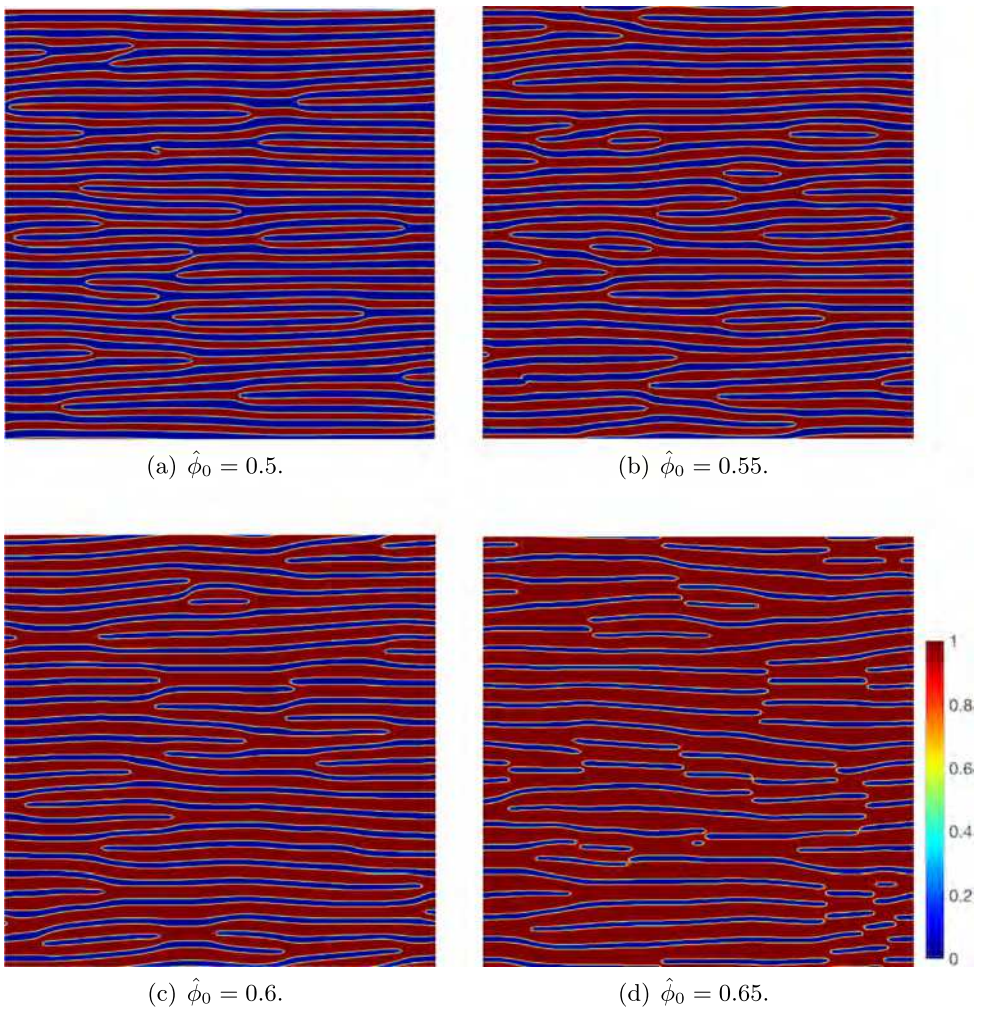

(a) $\hat{\phi}_0 = 0.5$. (b) $\hat{\phi}_0 = 0.55$.

(c) $\hat{\phi}_0 = 0.6$. (d) $\hat{\phi}_0 = 0.65$.

Fig. 4.17. The equilibrium solutions under the imposed electric field with the initial condition $\hat{\phi}_0 = 0.5, 0.55, 0.6$ and 0.65. The time step is $\delta t = 0.01$ and electric magnitude parameter is $\gamma = 5e3$.

Notice that the imposed electric term is linear, therefore we can simply modify (3.9) in the SSAV scheme as

$$\begin{aligned}\frac{3\phi^{n+1} - 4\phi^n + \phi^{n-1}}{2M\delta t} &- \epsilon^2 \Delta \phi^{n+1} + u^{n+1} H^{*,n+1} \\ &+ \beta \epsilon^2 (-\Delta)^{-1} \phi_{xx}^{n+1} + S(\phi^{n+1} - \phi^{*,n+1}) = 0.\end{aligned} \tag{4.7}$$

We still keep the computed domain $[0, 2\pi]^2$ and the initial condition (4.2), use the model parameters given in (4.3), and vary the magnitude of the electric field parameter γ to investigate the pattern formation due to electric effects. Note this model does not have any energy structure due to the imposed external electricity force.

In Fig. 4.16, we set $\gamma = 5e2$ and plot the snapshots of the phase-field variable ϕ at various times. We observe that phase dislocations gradually disappear and the final equilibrium solution presents curvy lamellar phase with a few dislocations. Then by varying the initial value of $\hat{\phi}_0 = 0.5, 0.55, 0.6, 0.65$ and increasing the magnitude of the electric field to $\gamma = 5e3$, we plot the final equilibrium solutions ($t = 2000$) in Fig. 4.17, we observe that various patterns of lamellar phases are obtained accordingly. All these obtained simulations are qualitatively consistent with the numerical results in [3,4,38].

5. Concluding remarks

In this paper, we develop a semi-discrete in time, easy-to-implement, and second-order scheme for solving the penalized Allen–Cahn type diblock copolymer model. At each time step, one only needs to solve two decoupled linear elliptic equations. The added linear stabilization term is shown to be crucial to enhance the stability and keep the

required accuracy when using large time steps. We further prove the unconditional energy stability of the developed scheme rigorously. Through the comparison with the non-stabilized SAV and first-order stabilized explicit scheme in simulating many numerical examples in 2D and 3D, we demonstrate the stability and the accuracy of the developed scheme numerically.

Acknowledgments

J. Zhang was partially supported by the National Natural Science Foundation of China (No. 11901132) and Science and Technology Program of Guizhou Province (No. [2020]1Y013); C. Chen was partially supported by NSFC-11771375, 11571297, and Shandong Province Natural Science Foundation ZR2018MAQ008. X. Yang was partially supported by National Science Foundation with Grant Nos. DMS-1720212 and DMS-1818783. K. Pan was supported by Science Challenge Project (No. TZ2016002), the National Natural Science Foundation of China (No. 41874086), the Excellent Youth Foundation of Hunan Province of China (No. 2018JJ1042).

References

[1] X. Xu, Y. Zhao, Energy stable semi-implicit schemes for Allen-Cahn-Ohta-Kawasaki model in binary system, J. Sci. Comput. 80 (2019) 1656–1680.
[2] T. Ohta, K. Kawasaki, Equilibrium morphology of block copolymer melts, Macromolecules 19 (10) (1986) 2621–2632.
[3] T. Xu, A.V. Zvelindovsky, G. Sevink A, O. Gang, B. Ocko, Y. Zhu, S.P. Gido, T.P. Russell, Electric field induced sphere-to-cylinder transition in diblock copolymer thin films, Macromolecules 37 (18) (2004) 6980–6984.
[4] Xiang-Fa Wu, Yuris A. Dzenis, Phase-field modeling of the formation of lamellar nanostructures in diblock copolymer thin films under inplanar electric fields, Phys. Rev. E 77 (3) (2008) 031807.
[5] R. Choksi, X. Ren, On the derivation of a density functional theory for microphase separation of diblock copolymers, J. Stat. Phys. 113 (2003) 151–176.
[6] S.A. Brazovskii, Phase transition of an isotropic system to a nonuniform state, JETP 41 (1) (1975) 85.
[7] L. Leibler, Theory of microphase separation in block copolymers, Macromolecules 13 (6) (1980) 1602–1617.
[8] G.H. Fredrickson, Surface ordering phenomena in block copolymer melts, Macromolecules 20 (6) (1987) 2535–2542.
[9] R. Choksi, M.A. Peletier, J.F. Williams, On the phase diagram for microphase separation of diblock copolymers: An approach via a nonlocal Cahn-Hilliard functional, SIAM J. Appl. Math 69 (2009) 1712–1738.
[10] D. Shirokoff, R. Choksi, J.C. Nave, Sufficient conditions for global minimality of metastable states in a class of non-convex functionals: A simple approach via quadratic lower bounds, J. Nonlinear Sci. 25 (2015) 539–582.
[11] R. Choksi, M. Maras, J.F. Williams, 2D phase diagram for minimizers of a Cahn-Hilliard functional with long-range interactions , SIAM J. Appl. Dyn. Syst. 10 (2011) 1344–1362.
[12] J.B. van den Berg, J.F. Williams, Validation of the bifurcation diagram in the 2D Ohta-Kawasaki problem , Nonlinearity 10 (2017) 1584–1638.
[13] J.B. van den Berg, J.F. Williams, Rigorously computing symmetric stationary states of the Ohta-Kawasaki problem in three dimensions , SIAM J. Math. Anal. 10 (2019) 131–158.
[14] J. Shen, X. Yang, Numerical approximations of Allen-Cahn and Cahn-Hilliard equations, Disc. Conti. Dyn. Sys.-A 28 (2010) 1669–1691.
[15] X. Feng, A. Prol, Numerical analysis of the Allen-Cahn equation and approximation for mean curvature flows, Numer. Math. 94 (2003) 33–65.
[16] S. Zhai, Z. Weng, X. Feng., Investigations on several numerical methods for the non-local Allen-Cahn equation, Int. J. Heat Mass Transfer 87 (2015) 111–118.
[17] Y. Gao, X. He, L. Mei, X. Yang, Decoupled, linear, and energy stable finite element method for Cahn-Hilliard-Navier-Stokes-darcy phase field model, SIAM. J. Sci. Comput. 40 (2018) B110–B137.
[18] X. Yang, G. Zhang, X. He, Convergence analysis of an unconditionally energy stable projection scheme for magneto-hydrodynamic equations, Appl. Numer. Math. 136 (2019) 235–256.
[19] J. Yang, S. Mao, X. He, X. Yang, Y. He, A diffuse interface model and semi-implicit energy stable finite element method for two-phase magnetohydrodynamics flows, Comput. Methods Appl. Mech. Engrg. 356 (2019) 435–464.
[20] D.J. Eyre, Unconditionally gradient stable time marching the cahn-hilliard equation, in: Computational and Mathematical Models of Microstructural Evolution (San Francisco, CA, 1998), in: Mater. Res. Soc. Sympos. Proc., 529, MRS, Warrendale, PA, 1998, pp. 39–46, MR1676409.
[21] A. Aristotelous, O. Karakashian, S.M. Wise, A mixed discontinuous Galerkin, convex splitting scheme for a modified Cahn-Hilliard equation and an efficient nonlinear multigrid solver, Discrete Contin. Dyn. Syst. B 18 (2013) 2211.
[22] H. Gomez, T.J.R. Hughes, Provably unconditionally stable, second-order time-accurate, mixed variational methods for phase-field models, J. Comput. Phys. 230 (2011) 5310–5327.
[23] H. Gomez, V.M. Calo, Y. Bazilevs, T.J.R. Hughes, Isogeometric analystis of the Cahn-Hilliard phase-field model, Comput. Methods Appl. Mech. Engrg. 197 (2008) 4333–4352.
[24] I. Romero, Thermodynamically consistent time stepping algorithms for nonlinear thermomechanical systems, Internat. J. Numer. Methods Engrg. 79 (2009) 706–732.
[25] D. Lee, J. Kim, Comparison study of the conservative Allen-Cahn and the Cahn-Hilliard equations., Math. Comput. Simulation 119 (2016) 35–56.
[26] X. Yang, Linear, first and second order and unconditionally energy stable numerical schemes for the phase field model of Homopolymer blends, J. Comput. Phys. 327 (2016) 294–316.
[27] X. Yang, J. Zhao, Q. Wang, J. Shen, Numerical approximations for a three components Cahn-Hilliard phase-field model based on the invariant energy quadratization method, Math. Models Methods Appl. Sci. 27 (2017) 1993–2030.
[28] J. Shen, J. Xue, J. Yang, The scalar auxiliary variable (SAV) approach for gradient flows, J. Comput. Phys. 353 (2018) 407–416.
[29] X. Yang, Numerical approximations for the Cahn-Hilliard phase field model of the binary fluid-surfactant system, J. Sci. Comput. 74 (2017) 1533–1553.
[30] X. Yang, Efficient linear, stabilized, second order time marching schemes for an anisotropic phase field dendritic crystal growth model, Comput. Methods Appl. Mech. Engrg. 347 (2019) 316–339.
[31] C. Chen, X. Yang, Efficient numerical scheme for a dendritic solidification phase field model with melt convection, J. Comput. Phys. 388 (2019) 41–62.
[32] C. Chen, X. Yang, Fast, provably unconditionally energy stable, and second-order accurate algorithms for the anisotropic Cahn-Hilliard model, Comput. Meth. Appl. Mech. Engrg 351 (2019) 35–59.

[33] J. Zhao, Q. Wang, X. Yang, Numerical approximations to a new phase field model for immiscible mixtures of nematic liquid crystals and viscous fluids, Comput. Methods Appl. Mech. Engrg. 310 (2016) 77–97.
[34] F.H. Lin, C. Liu, Global existence of solutions for the Ericksen Leslie–system, Arch. Rat. Mech. Ana. 154 (2) (2001) 135–156.
[35] Q. Du, C. Liu, X. Wang, A phase field approach in the numerical study of the elastic bending energy for vesicle membranes, J. Comput. Phys. 198 (2004) 450–468.
[36] K. Binder, Collective diffusion, nucleation, and spinodal decomposition in polymer mixtures, J. Chem. Phys. 79 (1983) 6387.
[37] M. Fialkowski, R. Holyst, Dynamics of phase separation in polymer blends revisited: Morphology, spinodal, noise, and nucleation, Macromol. Theory Simul. 17 (2008) 263.
[38] D. Jeong, J. Shin, Y. Li, Y. Choi, J-H. Jung, J. Kim S. Lee, Numerical analysis of energy-minimizing wavelengths of equilibrium states for diblock copolymers, Curr. Appl. Phys. 14 (2014) 1263–1272.